Supporting Information

Structural Ordering Enhances Highly Selective Low-Energy Production of Acetic Acid from CO_2

Shreya Sarkar,[a,b] Jithu Raj,[a,b] Debabrata Bagchi,[a,b] Arjun Cherevotan,[a,b]# C. P. Vinod[c], S. C. Peter[a,b]*

[a]*New Chemistry Unit, Jawaharlal Nehru Centre for Advanced Scientific Research, Jakkur, Bangalore-560064*
[b]*School of Advanced Materials, Jawaharlal Nehru Centre for Advanced Scientific Research, Jakkur, Bangalore-560064*
[c]Catalysis and Inorganic Chemistry Division, CSIR-National Chemical Laboratory, Dr. Homi Bhabha Road, Pune-411008

Experimental section

Chemicals

Chemicals used for the synthesis of the compounds: silver nitrate ($AgNO_3$, >99.99%), copper acetylacetonate ($Cu(acac)_2$, 99.9%), oleylamine (70%), selenium powder (Se, 99.9%) and sulfur powder (S, 99.99%) were purchased from Sigma Aldrich. Bismuth nitrate pentahydrate ($Bi(NO_3)_3.5H_2O$) (99.9%) was purchased from Alfa Aesar.

Synthesis

$MBiX_2$ catalysts were synthesized by colloidal method using oleylamine as the solvent and reducing agent. One mmol $AgNO_3$/$Cu(acac)_2$ was mixed in oleylamine and backflushed with N_2 for 15 minutes. After degassing the reaction mixture was heated to 60 °C until a transparent solution was produced. The reaction mixture was further heated to a temperature of 120 °C at which, 1 mmol $Bi(NO_3)_3.5H_2O$ dissolved in oleylamine was injected. The reaction temperature was further increased to 180 °C and was followed by S/Se injection. The reaction mixture was maintained at this temperature for 3 hours. The solution after being cooled to 60 °C was washed several times with a mixture of ethanol and *n*-hexane and was vacuum dried at 60 °C for 6 hours.

Characterization

Powder X-ray diffraction (PXRD): The PXRD measurements at room temperature were carried out on a Rigaku miniflex X-ray diffractometer using Cu-K_α as the X-ray source (λ = 1.5406 Å). The instrument is equipped with a position sensitive detector in the angular range $20^o \leq 2\theta \leq 90^o$ with the step size 0.02^o and scan rate of 1 sec/step calibrated against corundum standard. The experimental patterns were compared to the pattern simulated from Pearson's Crystal database.

Transmission Electron Microscopy (TEM): TEM images and selected area electron diffraction (SAED) patterns were collected using a JEOL JEM-2010 TEM instrument and color mapping was done in TECHNAI. The samples for these measurements were prepared by sonicating the nanocrystalline powders in ethanol and drop-casting a small volume onto a carbon-coated copper grid.

Scanning electron microscopy (SEM) and Energy Dispersive Spectrum (EDAX): The FESEM measurement was performed using FEI NOVA NANOSEM 600 scanning electron microscope equipped with an energy-dispersive X-ray spectroscopy (EDAX) instrument (Bruker 129 eV EDAX instrument). Data was acquired by using an accelerating voltage of 20 kV and typical time taken for data accumulation is 100 s. The elemental analyses were performed using the P/B-ZAF standardless method (where, P/B = peak to background model, Z = atomic no. correction factor, A = absorption correction factor and F = fluorescence factor) for C, N, O, Co at multiple areas on the sample coated Si wafer.

X-ray photoelectron spectroscopy (XPS): XPS measurements were carried out using Thermo K-alpha+ spectrometer using micro focused and monochromated Al Kα radiation with energy 1486.6 eV. The pass energy for spectral acquisition was kept at 50 eV for individual core-levels. The electron flood gun was utilized for providing charge compensation during data acquisition. Further, the individual core-level spectra were checked for charging using C1s at

284.6 eV as standard and corrected if needed. The peak fitting of the individual core-levels were done using XPSpeak 41 software with a Shirley type background. XPS spectra were measured to study the valence state, chemical composition and electronic interactions.

X-ray absorption near edge spectroscopy (XANES): XANES experiments at 300 K were performed at PETRA III, beamline P64, of DESY, Germany. Measurements of Pd-*K*, and Bi-L_{III} edges at ambient pressure were performed in fluorescence as well as transmission mode using gas ionization chambers to monitor the incident and transmitted X-ray intensities. Monochromatic X-rays were obtained using a Si (111) double crystal monochromator which was calibrated by defining the inflection point (first derivative maxima) of Cu foil as 8980.5 eV. The beam was focused by employing a Kirkpatrick-Baez (K-B) mirror optic. A rhodium-coated X-ray mirror was used to suppress higher order harmonics. A CCD detector was used to record the transmitted signals. Pellets for the ex-situ measurements were made by homogeneously mixing the sample with an inert cellulose matrix to obtain an X-ray absorption edge jump close to one.

Electrochemical measurements

General electrochemical set-up: All the electrochemical measurements were performed using a CHI 6008E electrochemical workstation. Electrochemical CO_2RR was carried out in a three-electrode system, which involves working electrode (glassy carbon or carbon cloth), counter electrode (graphitic carbon rod) and reference electrode (Ag/AgCl). The cell compartments (**Figure S11a** and **S11b**) are separated by a proton exchange membrane (Nafion 117) and the electrolyte used is 0.5 M $KHCO_3$ solution. The electrolyte solutions were purged with CO_2 gas for 1 hour prior to the measurement. The electrocatalyst was prepared by dispersing 2 mg of catalyst and 0.2 mg of Vulcan (activated carbon) in 200 µL of mixed solvent solution (IPA:H_2O = 1:1 v/v) and 10 µL of 1 wt% nafion binder. From the prepared catalyst 100 µL was coated on the carbon cloth and dried. The electrochemical cell was designed to have a large electrode

area (0.7 cm x 0.7 cm) and a small electrolyte volume (10 mL) in each of the two compartments, along with a gas headspace of approximately 10 mL above the electrolyte on each side of the membrane. The flow of CO_2 was regulated by a mass flow controller at 20 standard cubic centimetres per minute (sccm), flowed through the working electrode compartment of the cell during electrolysis. CO_2 flow through the cell was necessary in order to see large current efficiencies for CO_2 reduction products, presumably because of mass transport limitations in a quiescent cell. The flow rate of 20 sccm was chosen to ensure sufficient CO_2 transport to the surface while preventing interference from gas bubbles striking the surface.

Estimation of effective electrode surface area: According to reported literature, cyclic voltammetry (CV) can be used to determine the electrochemical double layer capacitance of different samples at non-Faradaic overpotentials for estimating the effective electrode surface areas. For that a series of CV measurements were performed at various scan rates (40, 60, 80, 100 and 120 mV s^{-1}) between -0.6 V to- 0.2 V vs. Ag/AgCl region, and the sweep segments of the measurements were set to 6 to ensure consistency. A linear trend was obtained from the plot of the difference of current density (1/2ΔJ) in the anodic and cathodic sweeps ($J_{anodic} - J_{cathodic}$) at 0.35 V vs. RHE against the scan rate. The slope of the fitting line is equal to twice the geometric double layer capacitance (C_{dl}), which is proportional to the effective electrode surface area of the materials. Therefore, the electrochemical surface areas of different samples can be compared with one another based on their C_{dl} values keeping other experimental condition same for each case.

Gaseous product analysis: All the gaseous products were analyzed by online 490-Micro Gas Chromatography (GC), which has four channels for detecting different gaseous products. Each channel has specific column for analyzing relevant gases *viz*. Molsieve 5Å (for channel 1 and 2), Pora PLOT U (in channel 3) and CP-Sil 5 CB (for channel 4). The carrier gases used were Ar and He. Each GC channel is equipped with a thermal conductivity detector (TCD). This

detector responds to the difference in thermal conductivity between a reference cell (carrier gas only) and a measurement cell (carrier gas containing sample components).

Calculation of Faradaic Efficiency (FE) for gaseous products,

$$FE_{gas} = \frac{ppm \times flow\ rate \times \frac{\#of\ electron \times Faradaic\ contant \times Pressu}{R \times Temperature}}{I_{average}}$$

Where *ppm* is the concentrations of individual gases detected by GC, *R* is the gas constant (0.082 L atm mol $^{-1}$K^{-1}), flow rate (mL min^{-1}) was measured by a universal flow meter (ADM 2000, Agilent Technologies) *of electron* is the number of transferred electrons for certain product, $I_{average}$ (A) is a steady-state current, *Faradaic constant* = 96 484 A.s.mol^{-1}, *Pressure* = 1.013 bar, *Temperature* = 273.15 K.

Liquid product analysis: The liquid products were analyzed by ^{1}H NMR (600 MHz, JEOL) and HPLC (Agilent 1220 Infinity II LC system). The following protocol was applied for the analysis. Fifty μL of the electrolyte and 30 μL of an internal standard solution were transferred into a centrifuge tube. The internal standard solution consisted of 50 mM phenol (99.5 %) and 10 mM dimethyl sulfoxide (99.9 %) made in D_2O solvent. The mixture is transferred into an NMR tube. Solvent suppression was used to decrease the intensity of the water peak.

The FEs of liquid products were calculated from the NMR and HPLC peak area.

$$FE_{liquid} = \frac{Concentration\ of\ Liquid \times V \times \#of\ electron \times Faradaic\ conta}{Charge}$$

Where *Concentration of Liquid* (mol.L^{-1}) was obtained from the previously calibrated NMR and HPLC, *V* (L) is the volume of the electrolyte, *Faradaic constant* = 96484 A.s.mol^{-1}, *Charge* (A.s) has been calculated from the chronoamperometry curve at the corresponding potential.

In-situ Electrochemical Fourier Transform Infrared Spectroscopy (FT-IR): In-situ electrochemical FT-IR spectroscopic studies were performed using a purged VERTEX FT-IR spectrometer equipped with the A530/P accessory and a mid-band MCT detector. A silicon hemispherical window (F530-8) was used with the working electrode placed 1 mm above the window as the single reflection attenuated total reflection (ATR) accessory for the FTIR study. The measurement parameters were 4 cm^{-1} resolution and 100 scans. This setup enabled the detection of eCO_2RR intermediate formation and change of adsorption of different intermediates on the electrode surface, as well as within the thin-layer electrolyte.

High-current density Flow-cell configuration: To increase the CO_2 diffusion and overall current density, the eCO_2RR experiments were carried out in a filter-press type Micro Flow Cell (Electrocell A/S), where a Ti sheet coated with IrMMO (iridium-mixed metal oxide) has been used as an Anode plate (Electrocell S/A). An anionic exchange membrane (Fumasep FAB-PK-130) was employed in the case of CO_2RR in 0.5M $KHCO_3$ medium and Ag/AgCl as the reference electrode. As shown in **Figure S40**, the cell has three compartments, (CO_2 gas, cathodic and anodic compartment). The electrolyte was recirculated continuously into the cell (both in cathode and anode) by two separate peristaltic pumps (Ravel, RH-P100L-100) to accumulate liquid products. The flow of CO_2 was regulated by a mass flow controller (Brooks) at different flowrate (standard cubic centimeters per minute (sccm)) to optimize the most suitable flow rate, flowed through the working electrode compartment of the cell during electrolysis. For the final study, the gas flow is fixed to 50 sccm, and electrolyte flow was set to 20 sccm. This flow has been optimized to prevent both the liquid and gas cross-over during the electrolysis through the GDE and maintain proper interface of gas-electrolyte and ion. For the product quantification and Faradaic efficiency calculation, chronoamperometric study for 1h has been performed at each individual potential.

Preparation of Gas-diffusion electrode (GDE): The gas diffusion electrode was fabricated by drop-casting the catalyst ink (catalyst dispersed in IPA with 1 wt.% Nafion) onto a 1*1 cm^2 of gas diffusion layer (GDL) (Freudenberg H23C2) which contains a microporous carbon black. After air-brushing, the GDE was left to dry overnight a room temperature and was electrochemically tested the next day. The electrode samples were weighed before and after catalyst deposition to determine the catalyst loading. The catalyst loading was determined to be approx. 1 mg cm^{-2}.

Tables

Table S1. Comparison of eCO_2RR performance for the production of acetic acid on various electrocatalysts reported in literature.

Catalyst	Electrolyte	Potential	Current density (mA cm-2)	Acetic acid (FE%)	Reference
$AgBiSe_2$	0.5M $KHCO_3$	-0.3V vs. RHE	15.8	49.81	*This work*
Mn-corrole complex	0.1M phosphate buffer ph=6	-0.67 vs. RHE	0.8	63	[3]
N-doped nanodiamond	0.5M $NaHCO_3$	-1.0V vs. RHE	1	77	[4]
In-SiW_9N_3	0.1M Na2SO4	0.71V vs. RHE	6	96.5	[5]
Cu doped Boron Nitride	1-ethyl-3-methylimidazolium tetrafluoroborate ([Emim]BF4)-LiI-water solution	-2.4V vs. Ag/AgCl	13.9	80.3	[6]

Table S2. The atomic coordinates and Wyckoff sites of $AgBiS_2$, $AgBiSe_2$ and $CuBiS_2$ catalysts.

Sample	Elements	Wyckoff site	Symmetry	x	y	z
$AgBiS_2$	0.5Ag +0.5Bi	4*a*	$m\bar{3}m$	0	0	0
	S	4*b*	$m\bar{3}m$	½	½	½
$AgBiSe_2$	Ag	3*a*	3*m*	0	0	0
	Bi	3*b*	-3*m*	0	0	½
	Se	6*c*	3*m*	0	0	0.231
$CuBiS_2$	Cu	4*c*	.*m*.	0.2509	¼	0.3281
	Bi	4*c*	.*m*.	0.26844	¼	0.56304
	S1	4*c*	.*m*.	0.3638	¼	0.902
	S2	4*c*	.*m*.	0.1258	¼	0.1777

Table S3. Faradaic efficiency of CO_2 reduced products on catalysts surface at different applied potential (vs. RHE) in H-cell configuration.

Catalyst	Product	FE (%) at different applied potential (vs. RHE)					
		−0.1 V	**−0.3 V**	**−0.5 V**	**−0.7 V**	**−0.9 V**	**−1.1 V**
$AgBiS_2$	CH_3COOH	12.55	32.70	35.97	12.08	2.17	1.14
	HCOOH	-	-	-	13.83	49.03	31.80
	CH_3OH	32.55	60.39	49.42	26.41	5.75	2.55
	CO	-	-	0.52	0.89	3.29	1.94
	CH_4	-	-	1.88	0.92	0.29	0.15
$AgBiSe_2$	CH_3COOH	21.50	37.18	13.27	5.15	0.97	1.53
	HCOOH	-	-	2.27	2.48	22.01	34.25
	CO	-	-	-	1.00	1.35	2.95
$CuBiS_2$	CH_3COOH	19.79	13.10	5.93	1.79	5.07	3.19
	HCOOH	-	-	4.45	21.33	21.66	9.58
	CO	-	-	-	0.46	0.76	0.44

Table S4. Vibrational frequencies of various surface bound species during CO_2 reduction.

Sl No	Vibrational frequency (cm^{-1})	Moiety	Vibration mode	Catalyst
1	1650	COOH	C=O stretch	Ag[1]
2	1386	COOH	C-O stretch	Ag[1]
3	1288	COOH	O-H deformation	Ag[1]
4	1410	COO^-	Symmetric stretch	Ag[1]
5	1560	COO^-	Asymmetric stretch	Ag[1]
6	1217	COH	C-O stretch	Mn porphyrin[2]
7	1116	COH	C-O stretch	Mn porphyrin[2]
8	1477	HCO	C=O stretch	Cu[3]
9	1390	OCH_3	C-H bend	Cu[3]

10	1240	HCOO	Symmetric C=O stretch	Cu[3]
11	1380	COOH	C-O stretch	Cu[4]

Table S5. Faradaic efficiency of CO_2 reduced products on catalysts surface at different applied potential (vs. RHE) in Flow-cell configuration.

Catalyst	**Product**	**FE (%) at different applied potential (vs. RHE)**					
		−0.1 V	**−0.3 V**	**−0.5 V**	**−0.7 V**	**−0.9 V**	**−1.1 V**
$AgBiS_2$	CH_3COOH	22.23	39.56	40.68	22.32	12.65	10.45
	HCOOH	-	-	-	20.67	42.38	46.67
	CH_3OH	49.32	53.47	39.82	27.37	6.82	5.52
	CO	-	-	0.86	0.89	6.58	6.72
	CH_4	-	-	2.83	1.34	0.35	0.57
$AgBiSe_2$	CH_3COOH	35.54	49.81	27.82	15.55	14.27	10.53
	HCOOH	-	-	9.87	15.85	28.16	38.64
	CO	5.35	6.75	7.85	8.95	7.58	9.94
$CuBiS_2$	CH_3COOH	37.53	28.82	19.32	15.26	12.93	10.47
	HCOOH	4.45	5.78	6.88	29.73	31.46	29.48
	CO	4.56	6.76	8.32	7.46	7.76	8.43

Figures

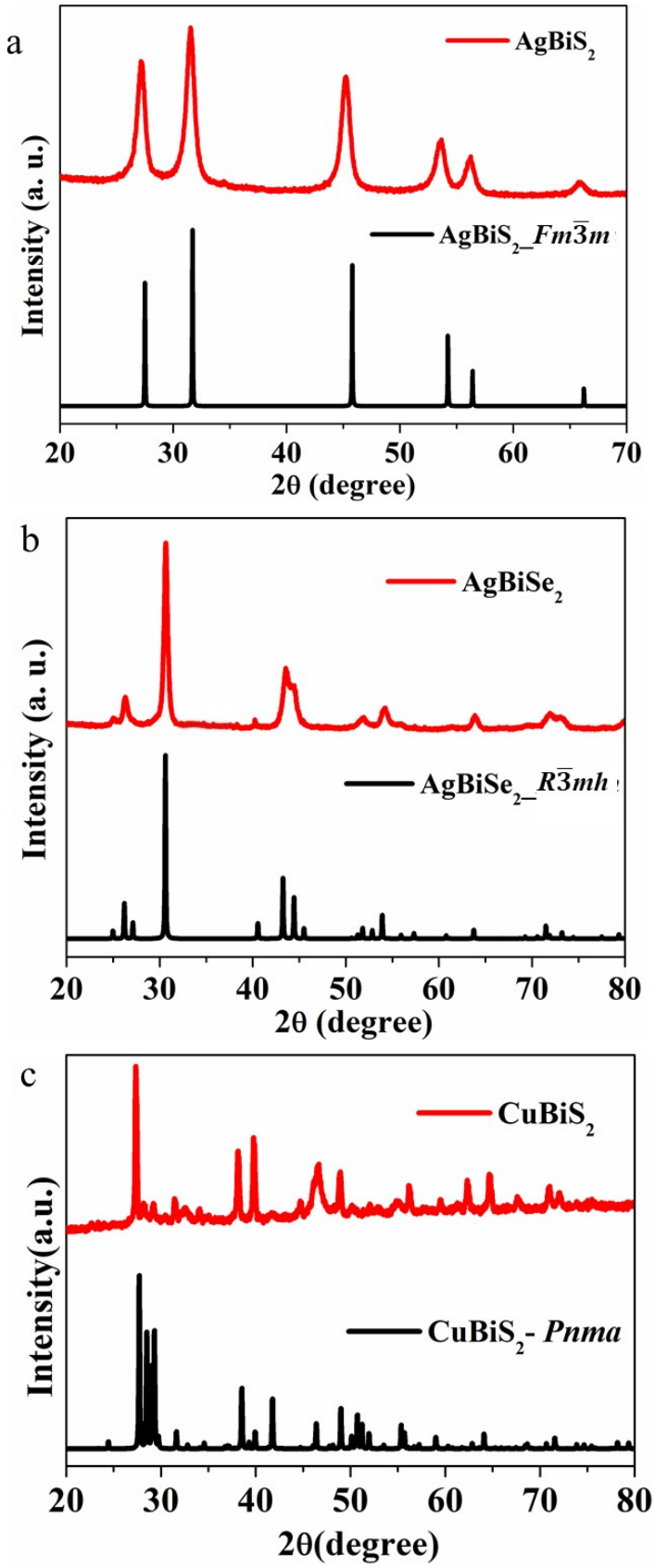

Figure S1. PXRD pattern of **(a)** $AgBiS_2$, **(b)** $AgBiSe_2$ and **(c)** $CuBiS_2$ matched with their respective simulated pattern.

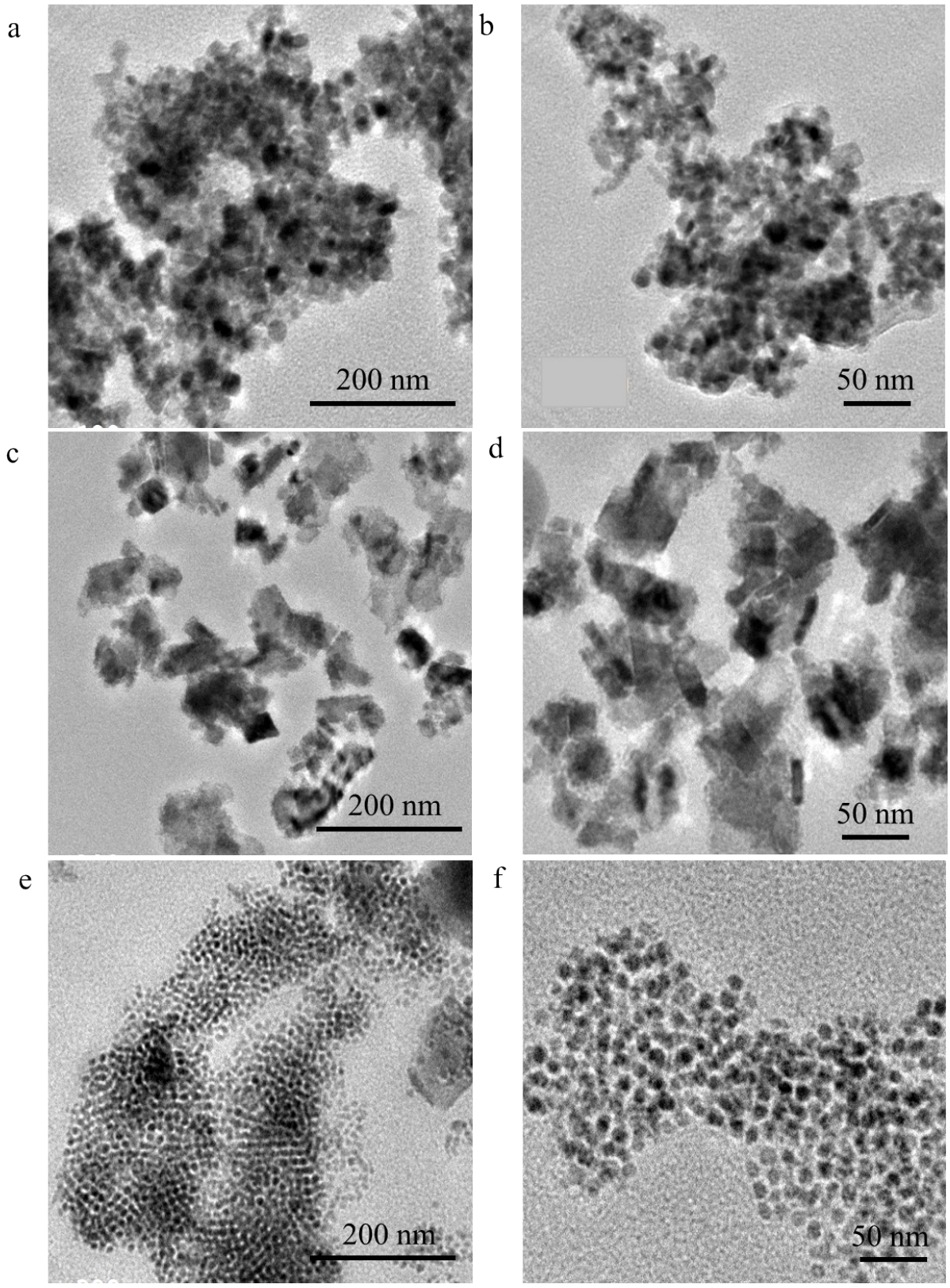

Figure S2. TEM images of $AgBiS_2$ (**a** and **b**), $AgBiSe_2$ (**c** and **d**) and $CuBiS_2$ (**e** and **f**).

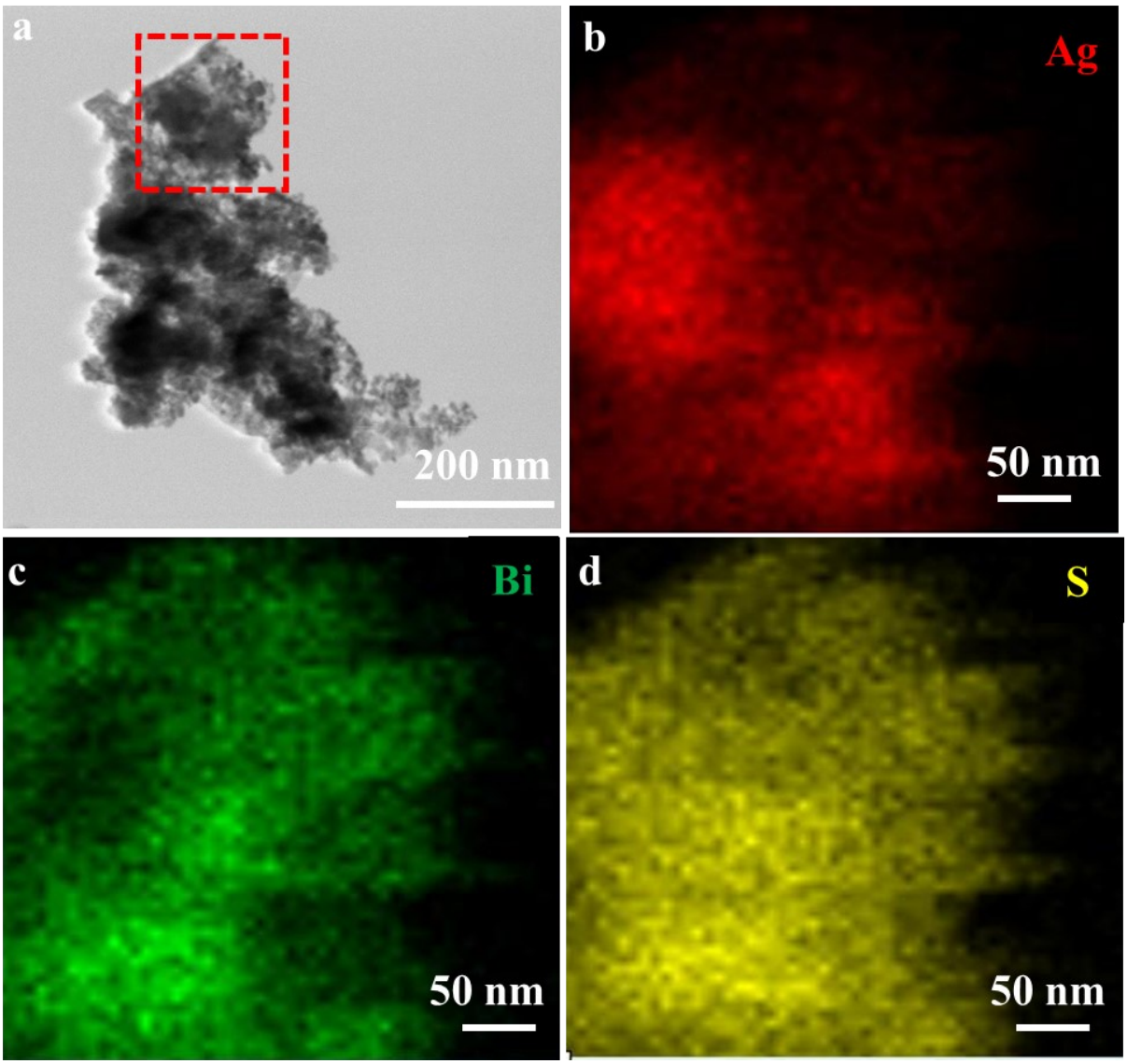

Figure S3. (a) Bright field STEM image and elemental mapping of $AgBiS_2$: **(b)** Ag, **(c)** Bi and **(d)** S.

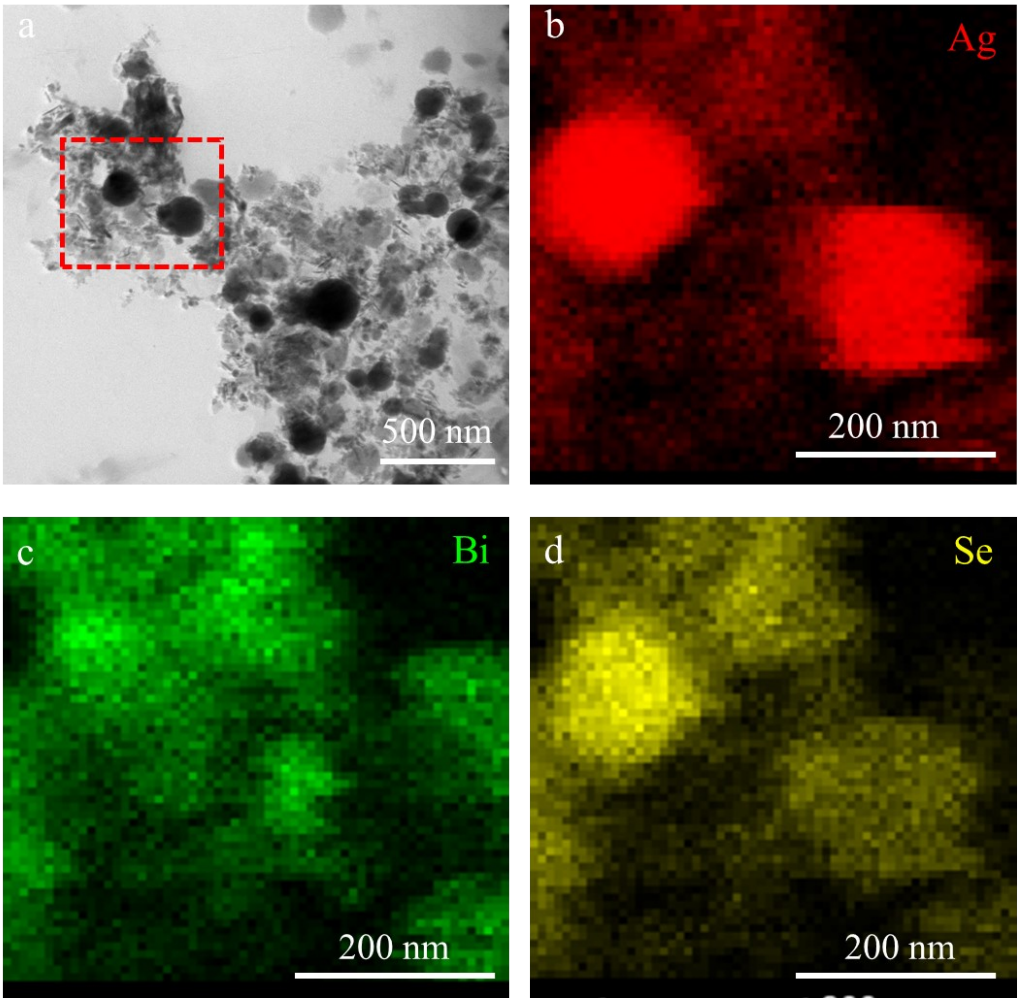

Figure S4. (a) Bright field STEM image and elemental mapping of $AgBiSe_2$: **(b)** Ag, **(c)** Bi and **(d)** Se.

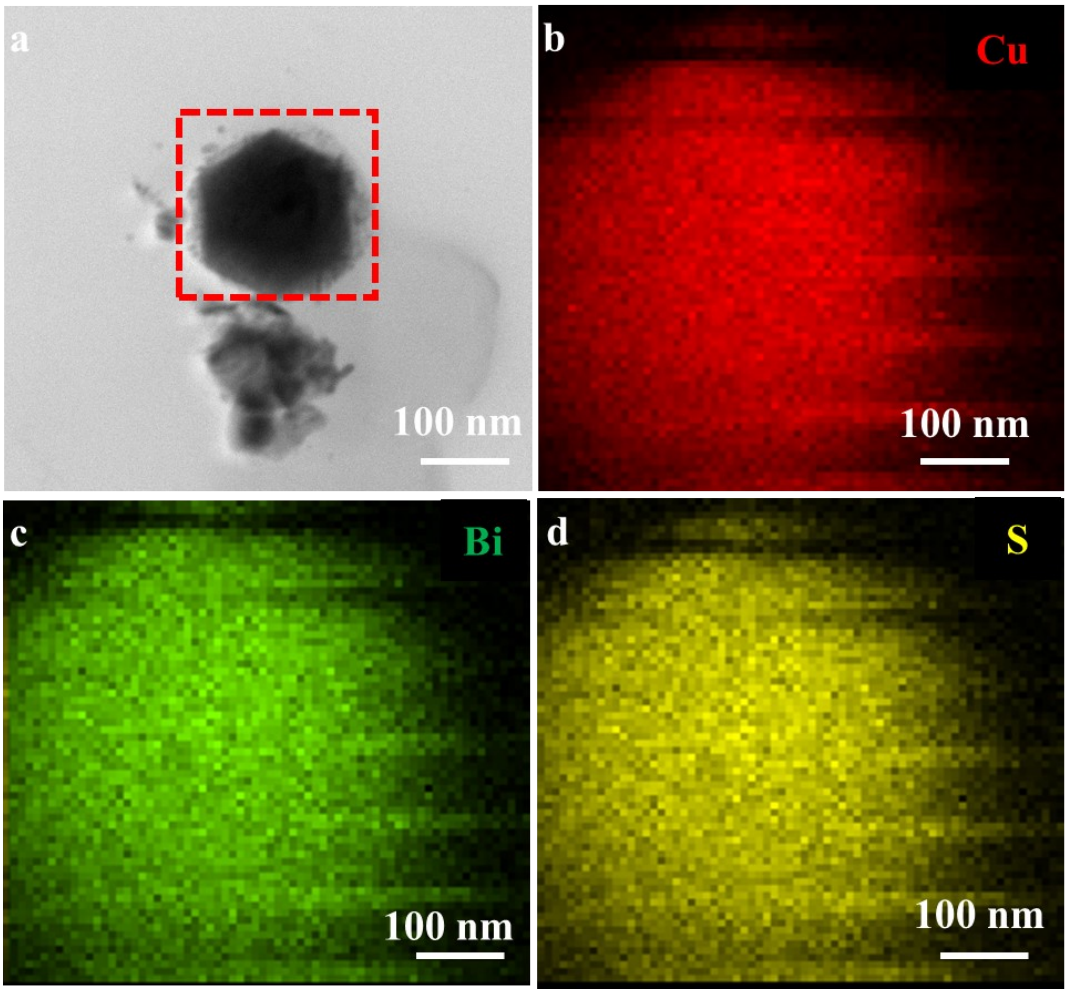

Figure S5. (a) Bright field STEM image and elemental mapping of $CuBiS_2$:**(b)** Cu, **(c)** Bi and **(d)** S.

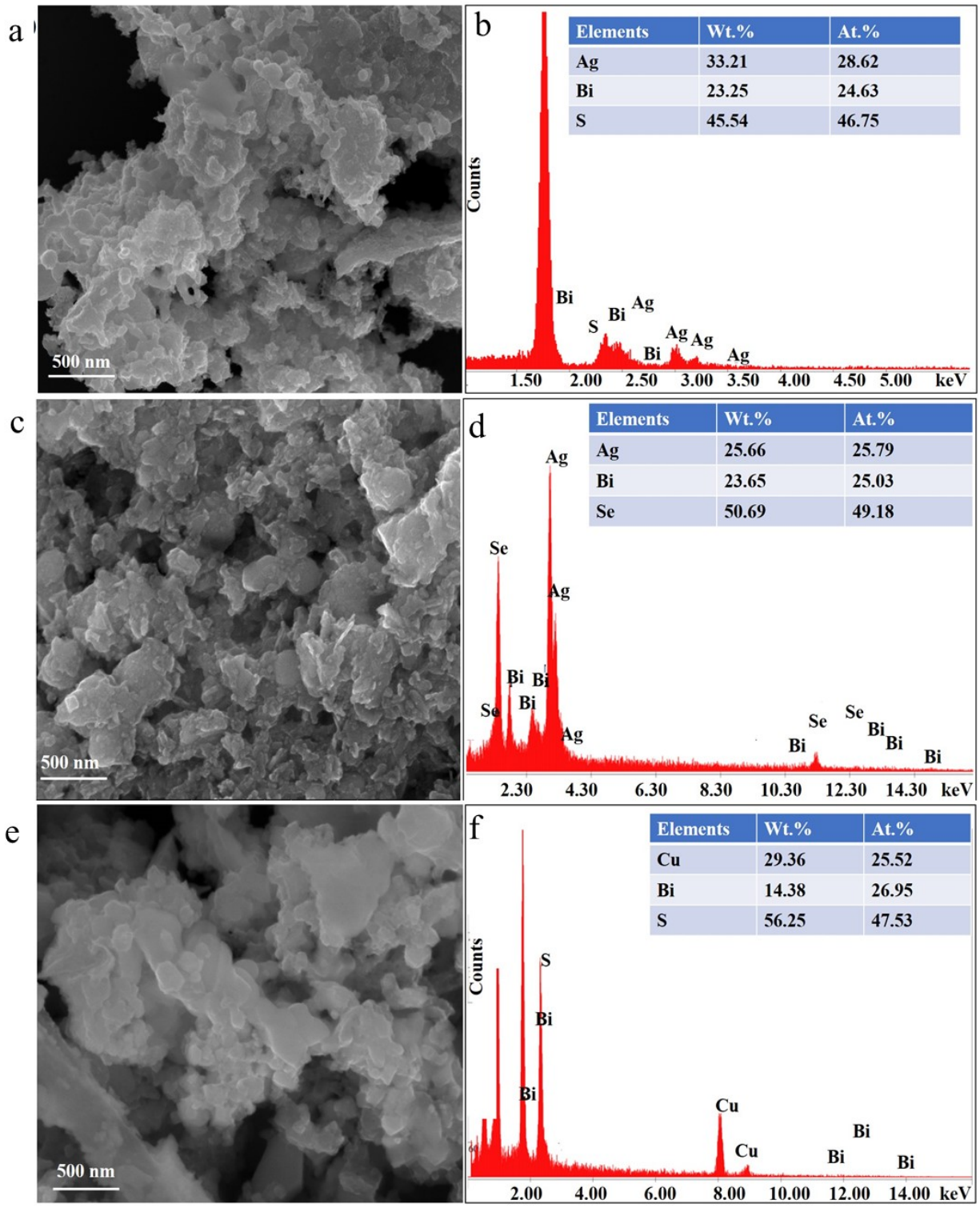

Figure S6. FESEM image of (**a**) $AgBiS_2$, **(c)** $AgBiSe_2$ and **(e)** $CuBiS_2$. EDAX spectra of (**b**) $AgBiS_2$, **(d)**, $AgBiSe_2$ and **(f)** $CuBiS_2$. Inset of (EDAX spectra represents the elemental composition.

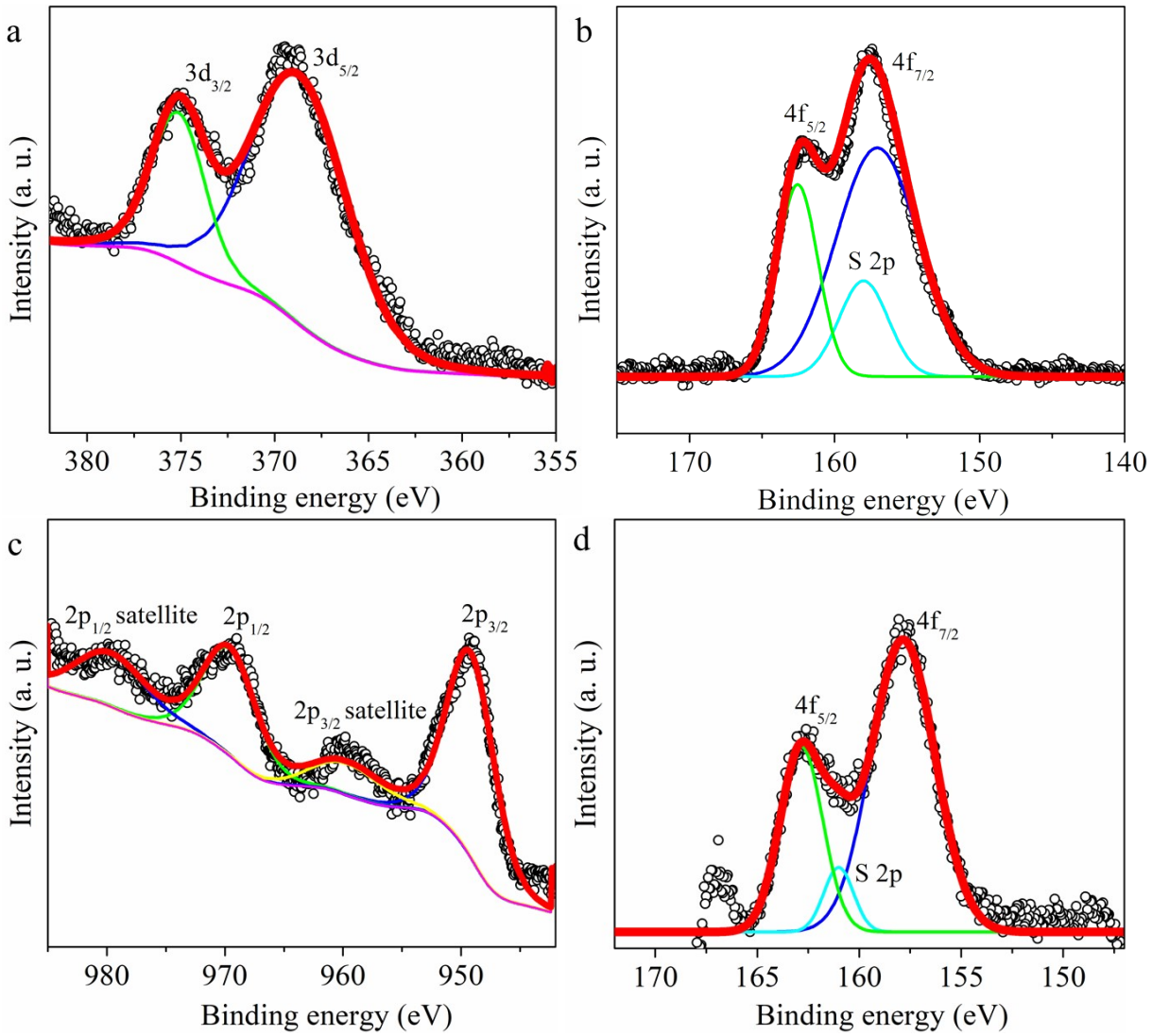

Figure S7. XPS spectra of $AgBiS_2$ nanoparticle **(a)** Ag 3*d* and **(b)** Bi 4*f* and $CuBiS_2$ nanoparticle **(c)** Cu 2*p* and **(d)** Bi 4*f* and S 2*p*.

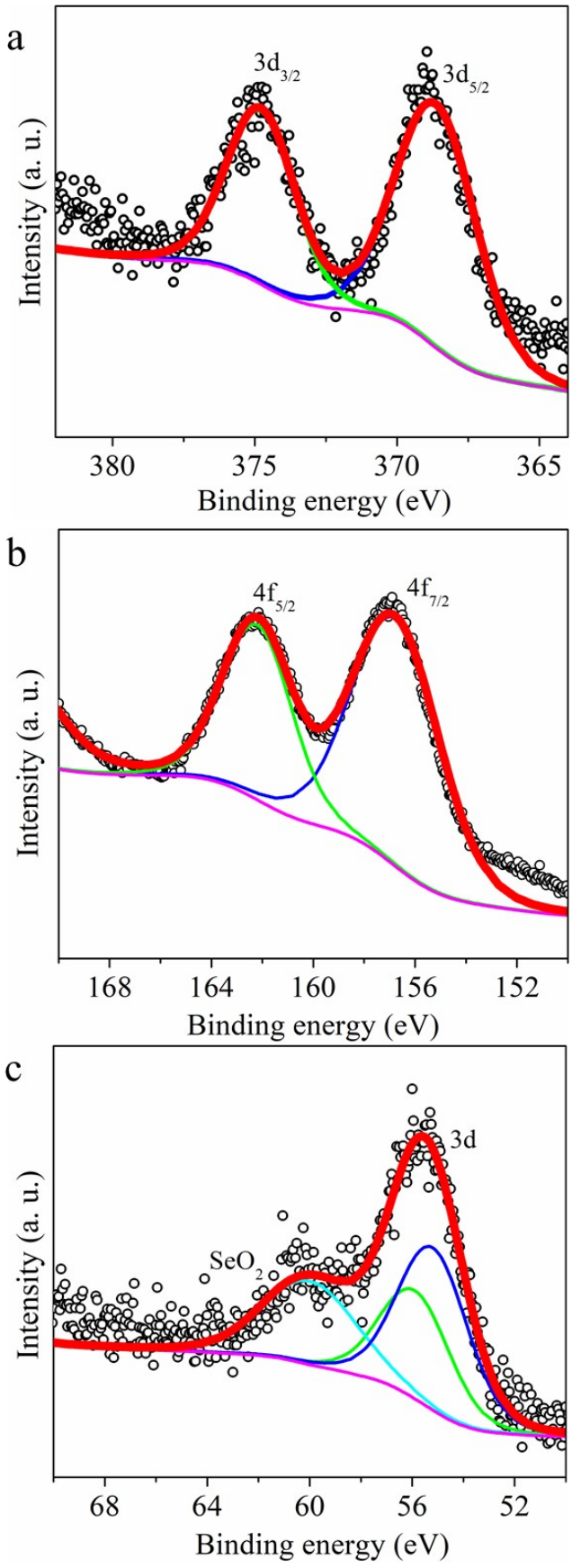

Figure S8. XPS spectra of $AgBiSe_2$ nanoparticles **(a)** Ag 3*d*, **(b)** Bi 4*f* and **(c)** Se 3*d* states respectively.

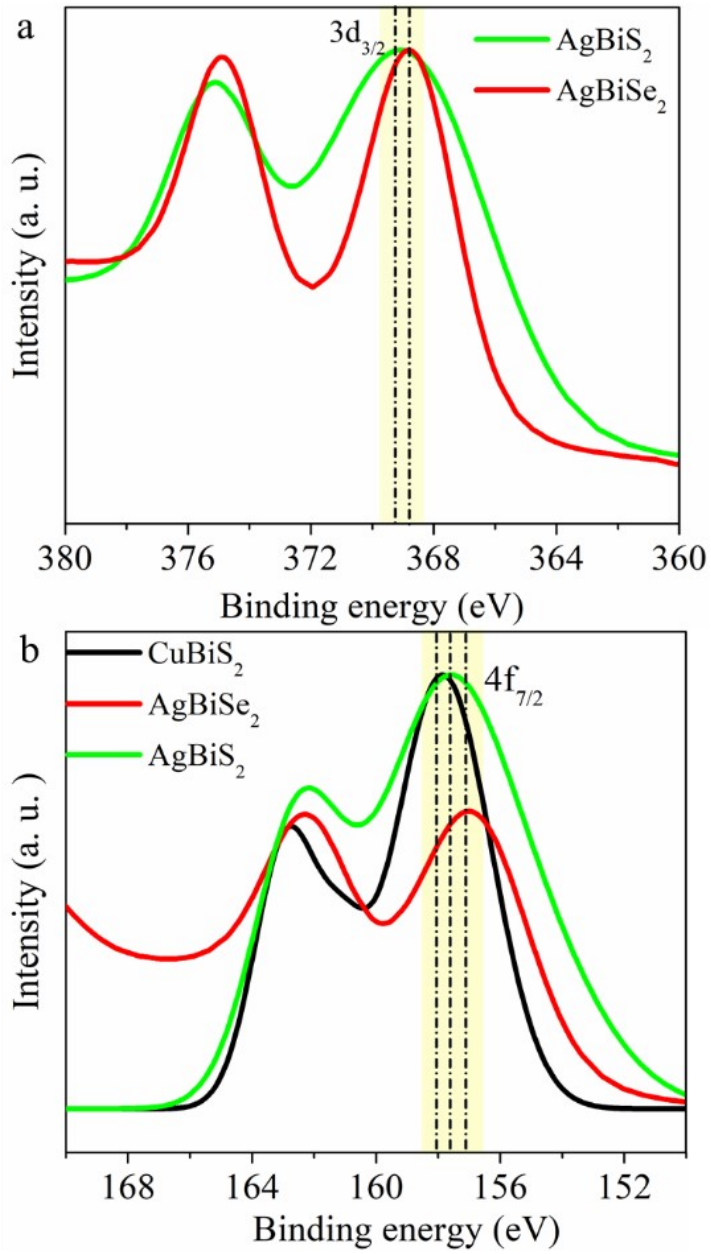

Figure S9. Comparison of XPS spectra of $AgBiS_2$, $AgBiSe_2$ and $CuBiS_2$ nanoparticles **(a)** Ag 3*d* and **(b)** Bi 4*f*.

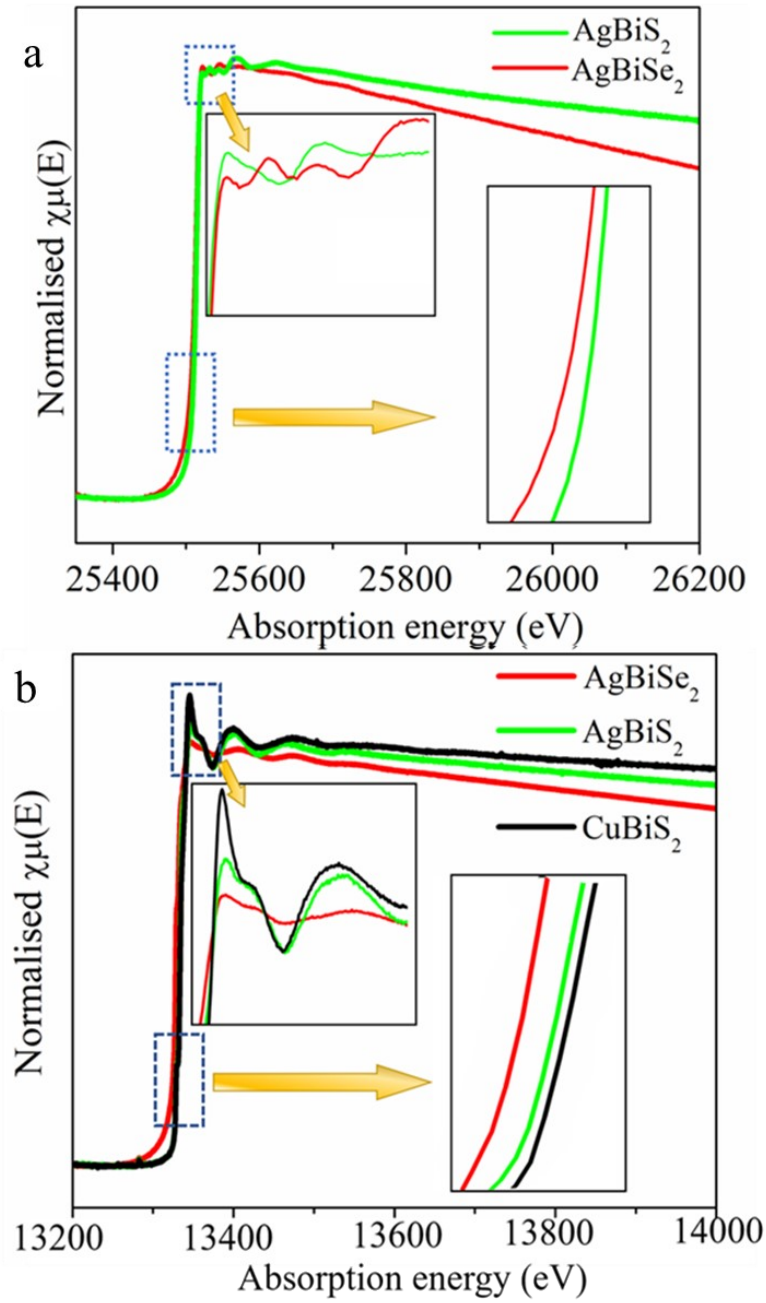

Figure S10. XANES spectra of **(a)** Ag-*K* edge and **(b)** Bi-L_{III} edge for $AgBiS_2$, $AgBiSe_2$ and $CuBiS_2$ nanoparticles. Individual figure insets show the zoomed in portion of the respective absorption edge and white-line intensity.

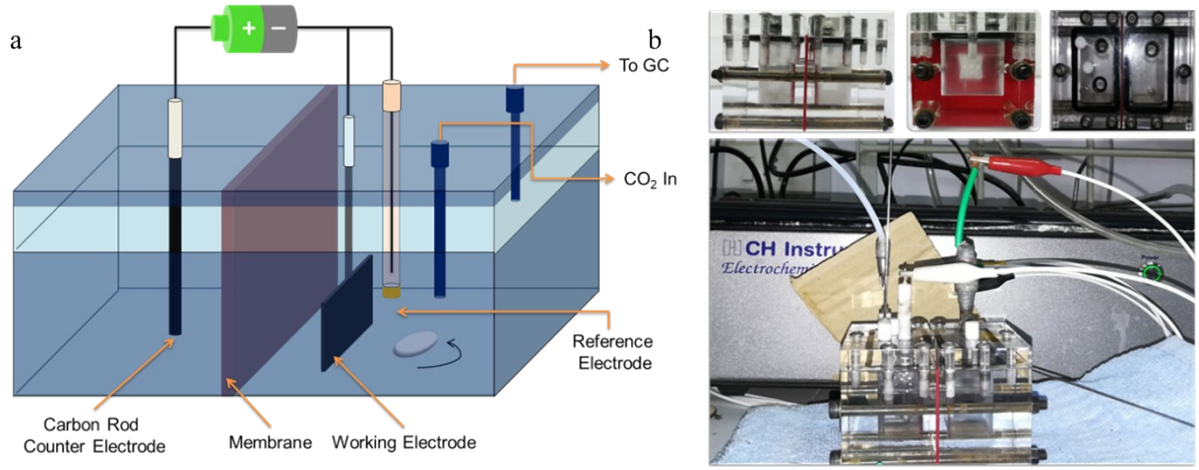

Figure S11. (a) Schematic illustration of the electrochemical reactor used for eCO_2RR. **(b)** Optical image of the reactor used in eCO_2RR.

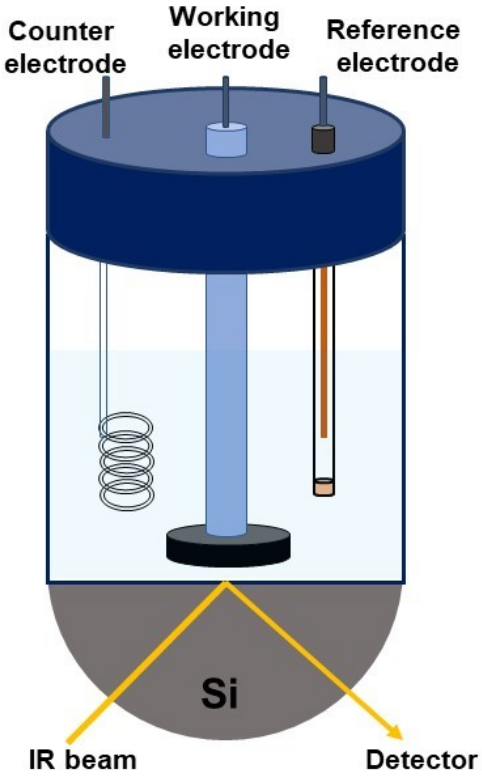

Figure S12. Schematic illustration of in-situ FT-IR configurations for eCO_2RR.

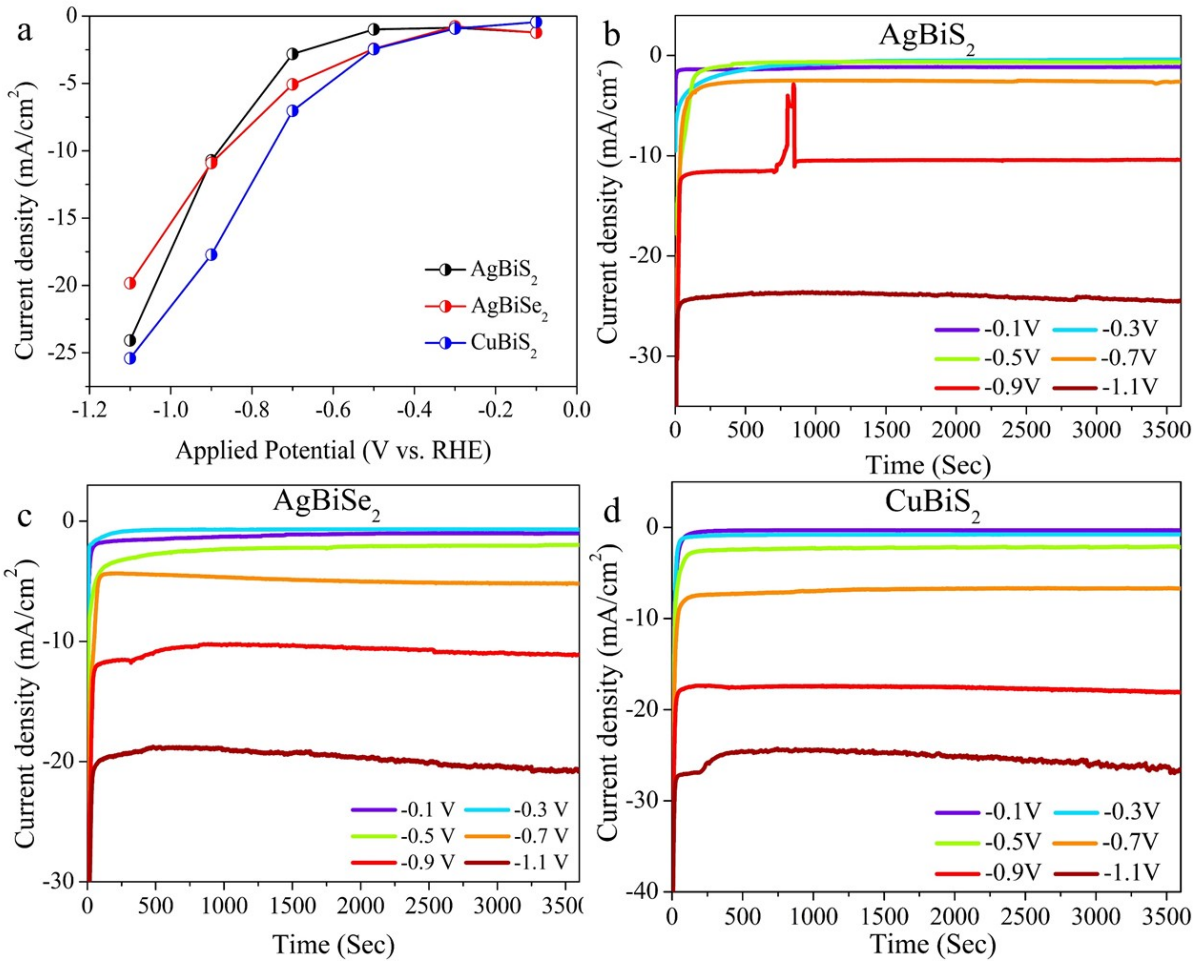

Figure S13. (a) Current density vs. applied potential on different chalcogenide catalysts. Chronoamperometry for **(b)** $AgBiS_2$, **(c)** $AgBiSe_2$ and **(c)** $CuBiS_2$ at different potentials in CO_2-saturated 0.5 M $KHCO_3$ in eCO_2RR for 1 h.

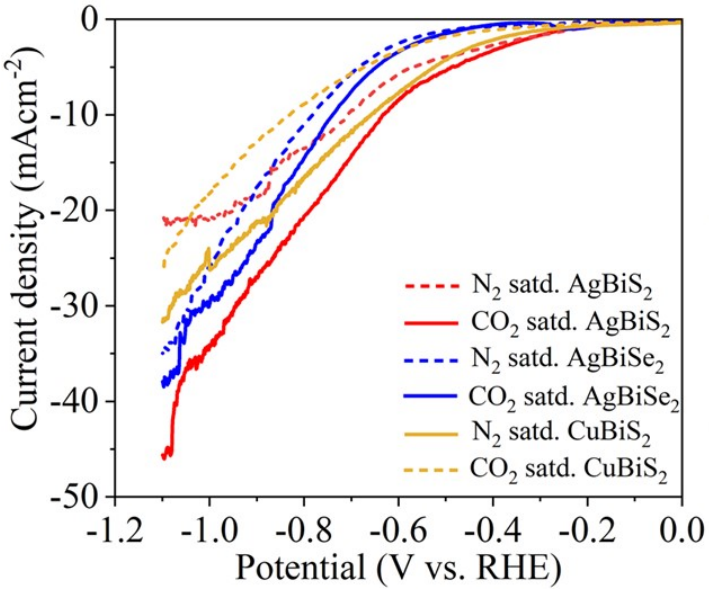

Figure S14. LSV polarization of $AgBiS_2$, $AgBiSe_2$ and $CuBiS_2$ electrocatalysts in N_2 and CO_2 atmosphere at a scan rate of 5 mV/sec. Solid and dotted lines represent the polarization curves in CO_2 atmosphere and N_2 atmosphere. The measurement was done in a normal 3-electrode glass cell using Ag/AgCl as the reference electrode, graphite rod as the counter electrode and 3 mm glassy carbon as the working electrode.

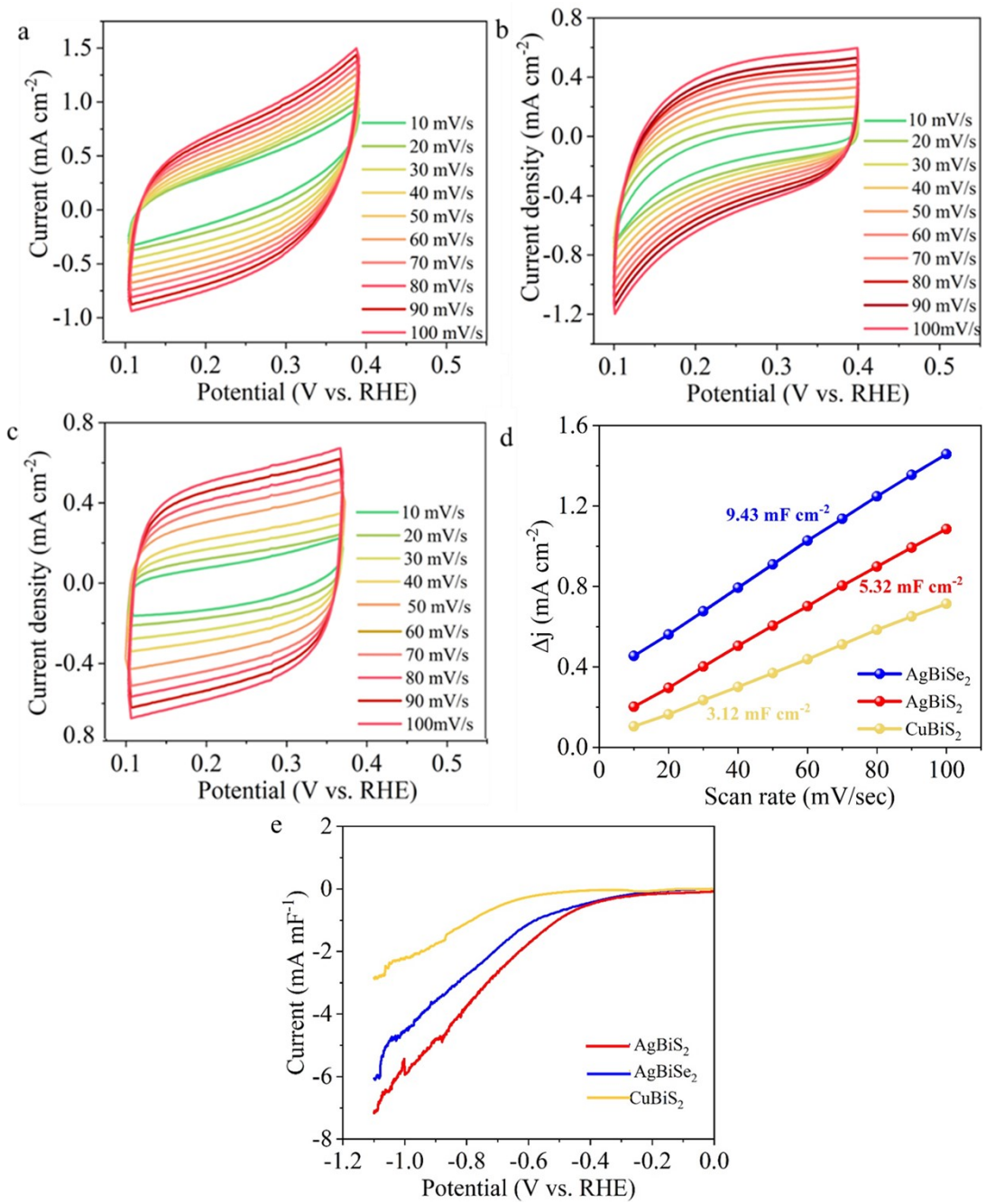

Figure S15. Cyclic voltammograms (CVs) of **(a)** $AgBiS_2$, **(b)** $AgBiSe_2$ and **(c)** $CuBiS_2$ sweeping over the potential from 0.1 V to 0.4 V (vs. RHE) for the determination of double-layer capacitance (C_{dl}) and thereby estimation if effective surface area (ECSA), **(d)** Plots of ΔJ vs. scan rate for $AgBiS_2$, $AgBiSe_2$ and $CuBiS_2$ where slope of the fitted line gives the corresponding C_{dl} values and (e) LSV polarization curves of $AgBiS_2$, $AgBiSe_2$ and $CuBiS_2$ catalysts normalized with respect to C_{dl} values as obtained from figure S15d.

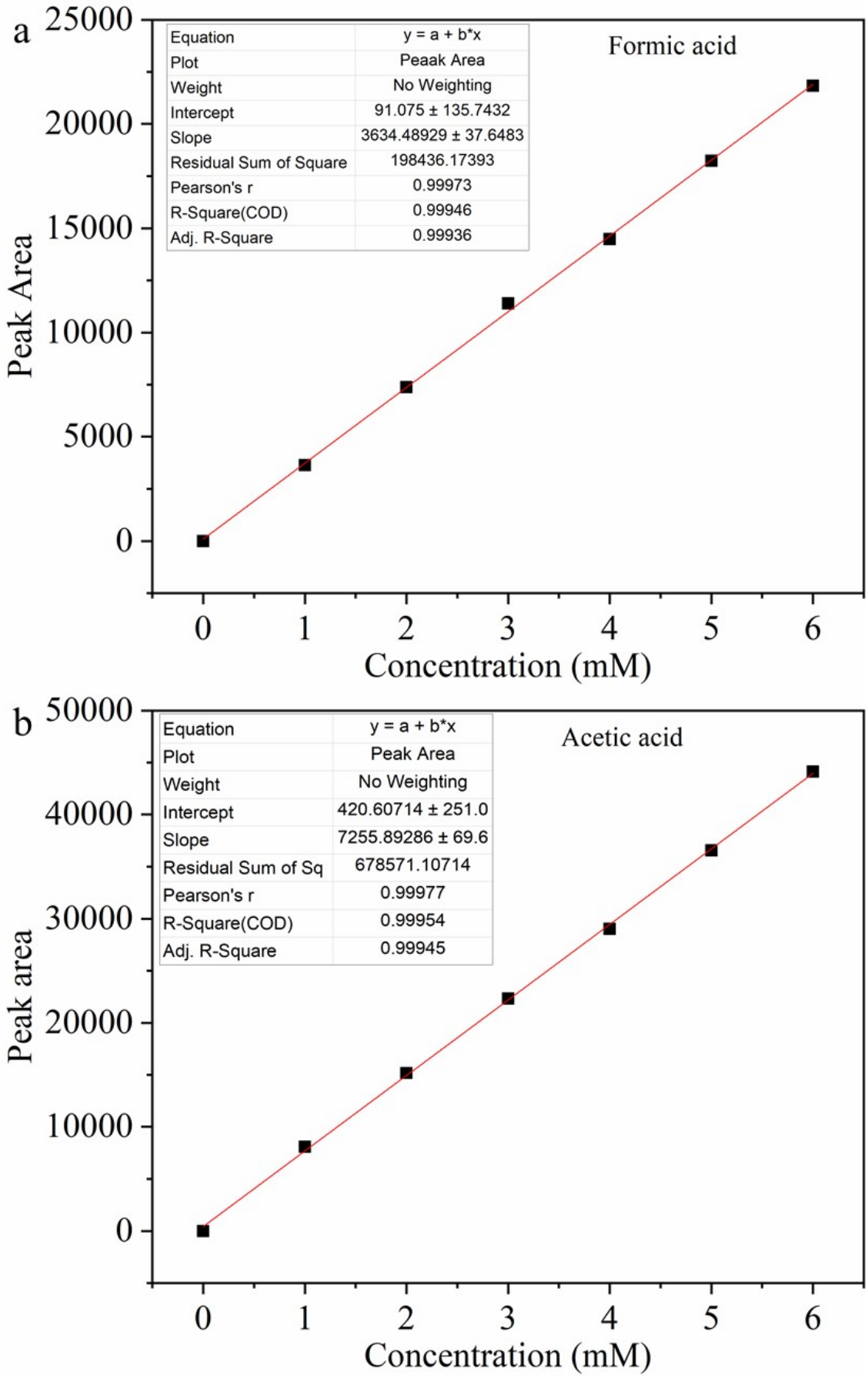

Figure S16. HPLC calibration curves of **(a)** formic acid, and **(b)** acetic acid.

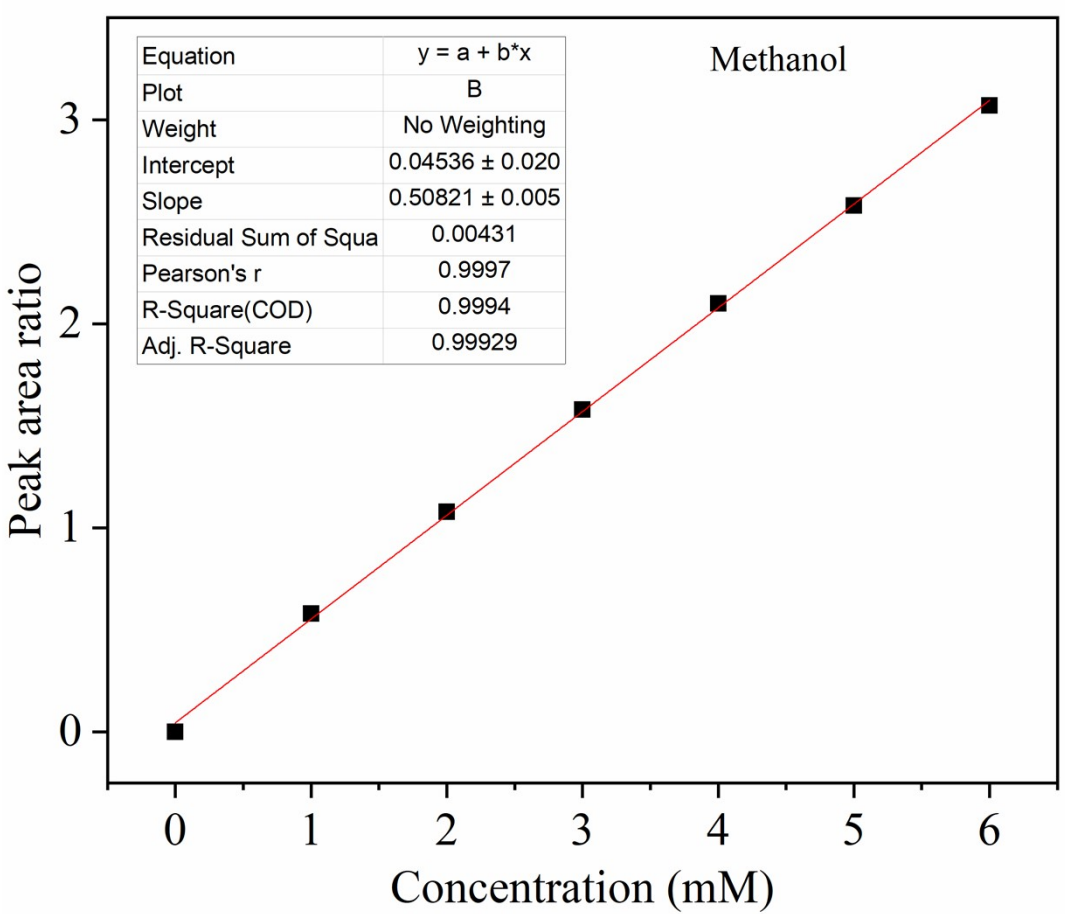

Figure S17. 1H-NMR calibration curves of Methanol.

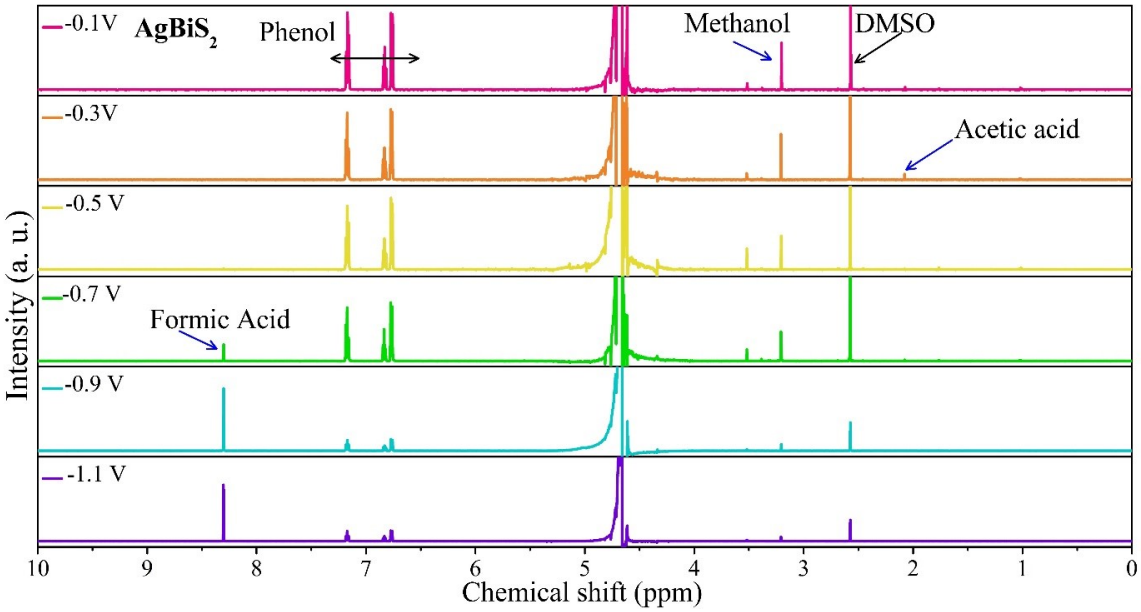

Figure S18. NMR spectra of the catholyte obtained from the CO_2 reduction at each individual potential. Experimental conditions: $AgBiS_2$ as working electrode with 0.5 M $KHCO_3$ electrolyte at the end of CA measured at different potentials.

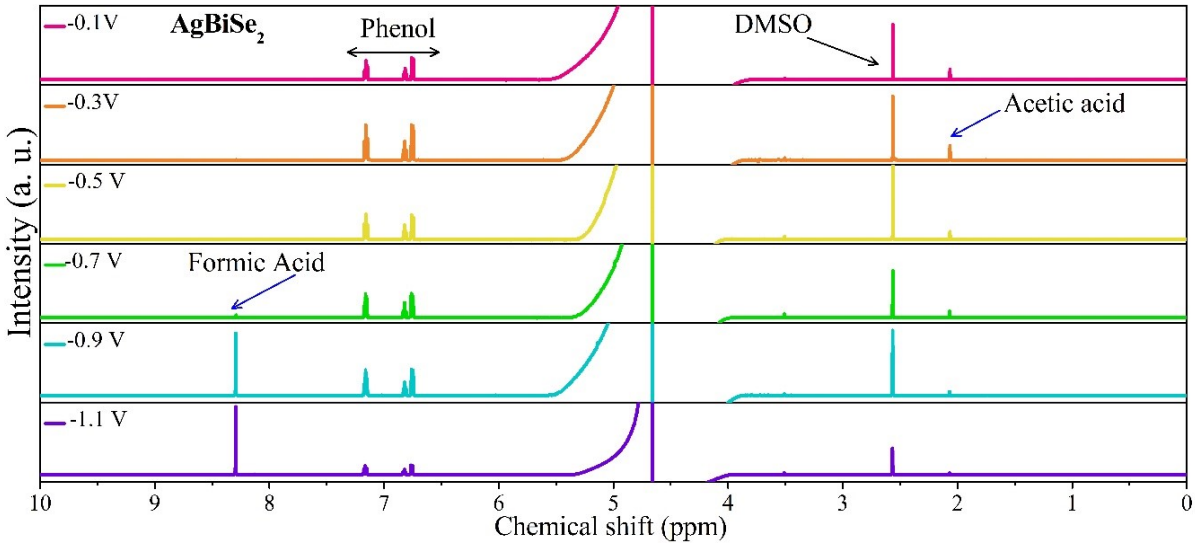

Figure S19. NMR spectra of the catholyte obtained from the CO_2 reduction at each individual potential. Experimental conditions: $AgBiSe_2$ as working electrode with 0.5 M $KHCO_3$ electrolyte at the end of CA measured at different potentials.

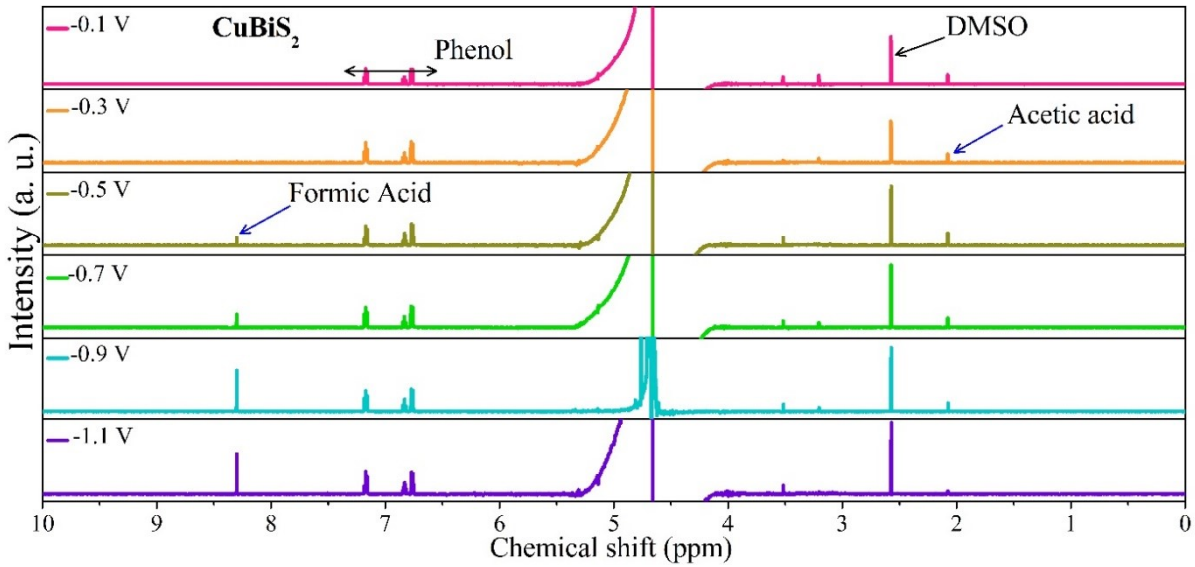

Figure S20. NMR spectra of the catholyte obtained from the CO_2 reduction at each individual potential. Experimental conditions: $CuBiS_2$ as working electrode with 0.5 M $KHCO_3$ electrolyte at the end of CA measured at different potentials.

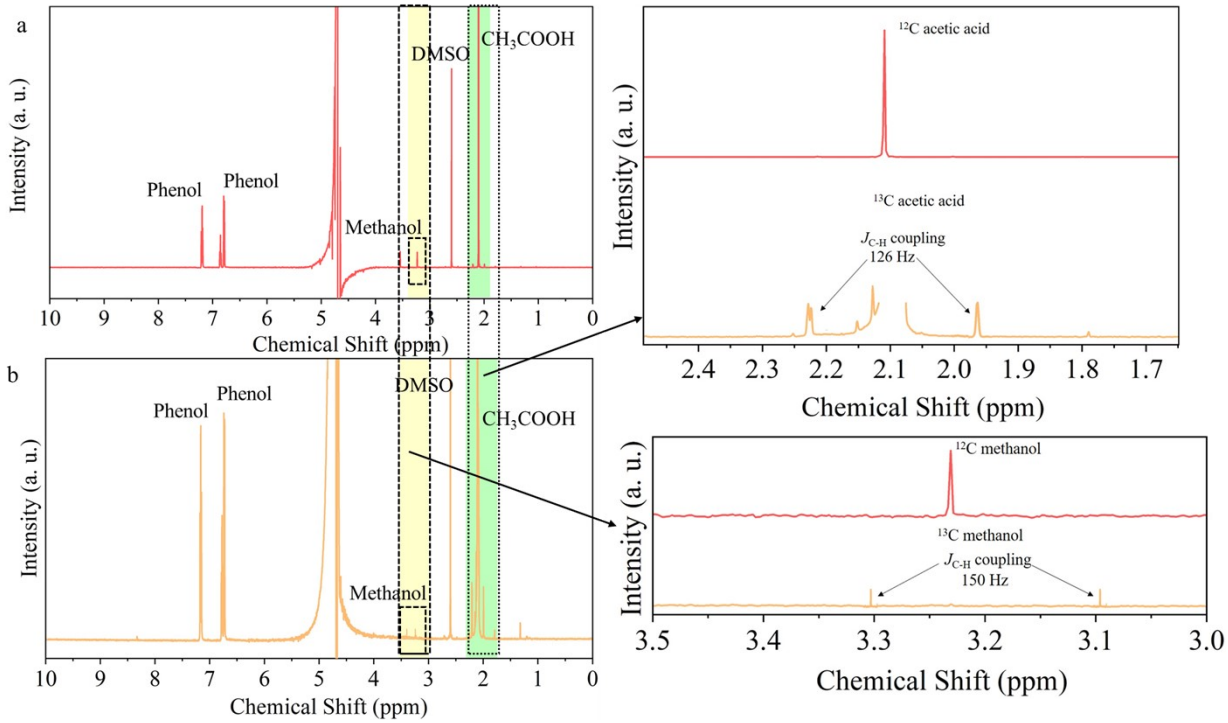

Figure S21. ^{1H} NMR spectra of electrolyte solutions after CO_2 electrolysis on $AgBiS_2$ catalyst using $^{12}CO_2$ (a) and $^{13}CO_2$ (b) as the feedstock in CO_2 saturated 0.5M $KHCO_3$ at -0.3V vs. RHE.

^{1H} NMR spectra demonstrates the splitting of H atoms of acetic acid and methanol by 13C atom. It can be observed that H peaks distributes symmetrically on both sides of H-^{12}C. Only ^{13}C signal for acetic acid and methanol could be observed from the ^{1H} NMR spectra indicating that both acetic acid and methanol were derived from CO_2 and not from any other chemicals.

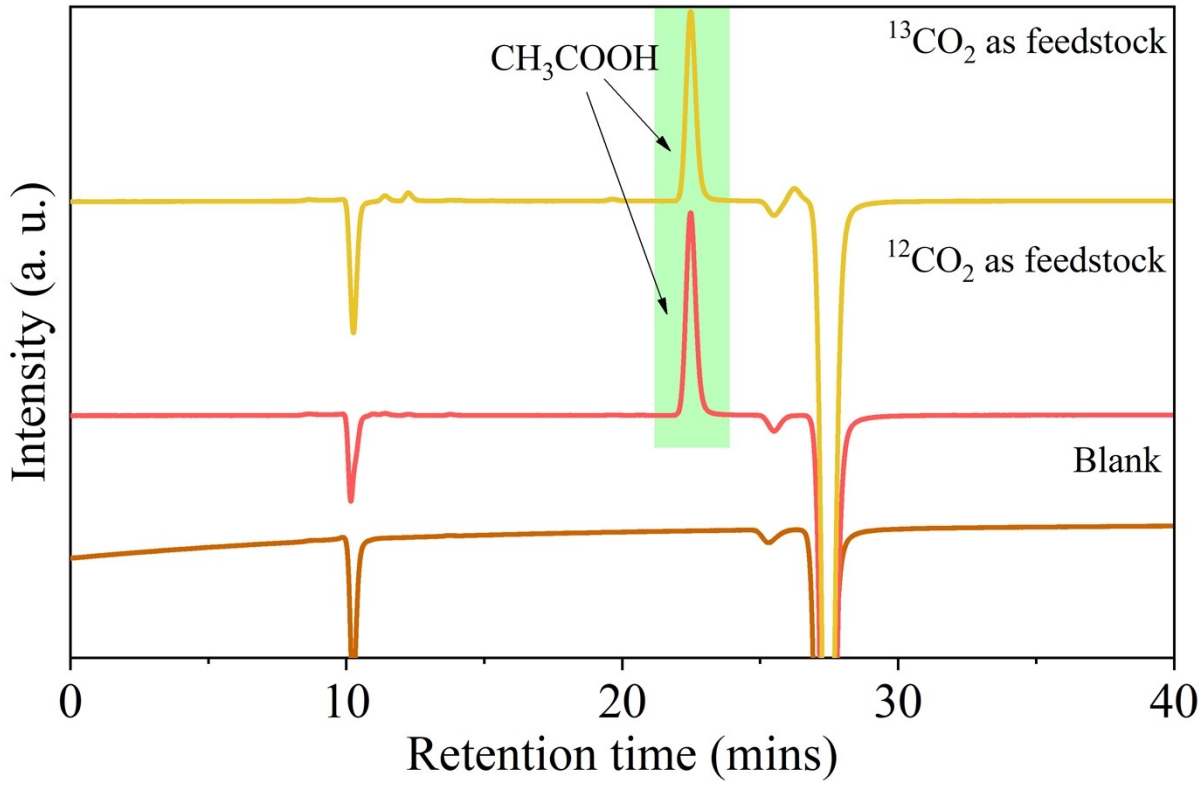

Figure S22. HPLC spectra after CO_2 electrolysis on $AgBiS_2$ catalyst using both $^{12}CO_2$ and $^{13}CO_2$ as feedstock at potential of -0.1V vs. RHE.

HPLC spectra shows the presence of acetic acid when both $^{12}CO_2$ and $^{13}CO_2$ is used as the feedstock at the same retention time indicating acetic acid is produced from CO_2 and not from any other chemicals. However, due to our instrumental limitation methanol cannot be detected using HPLC.

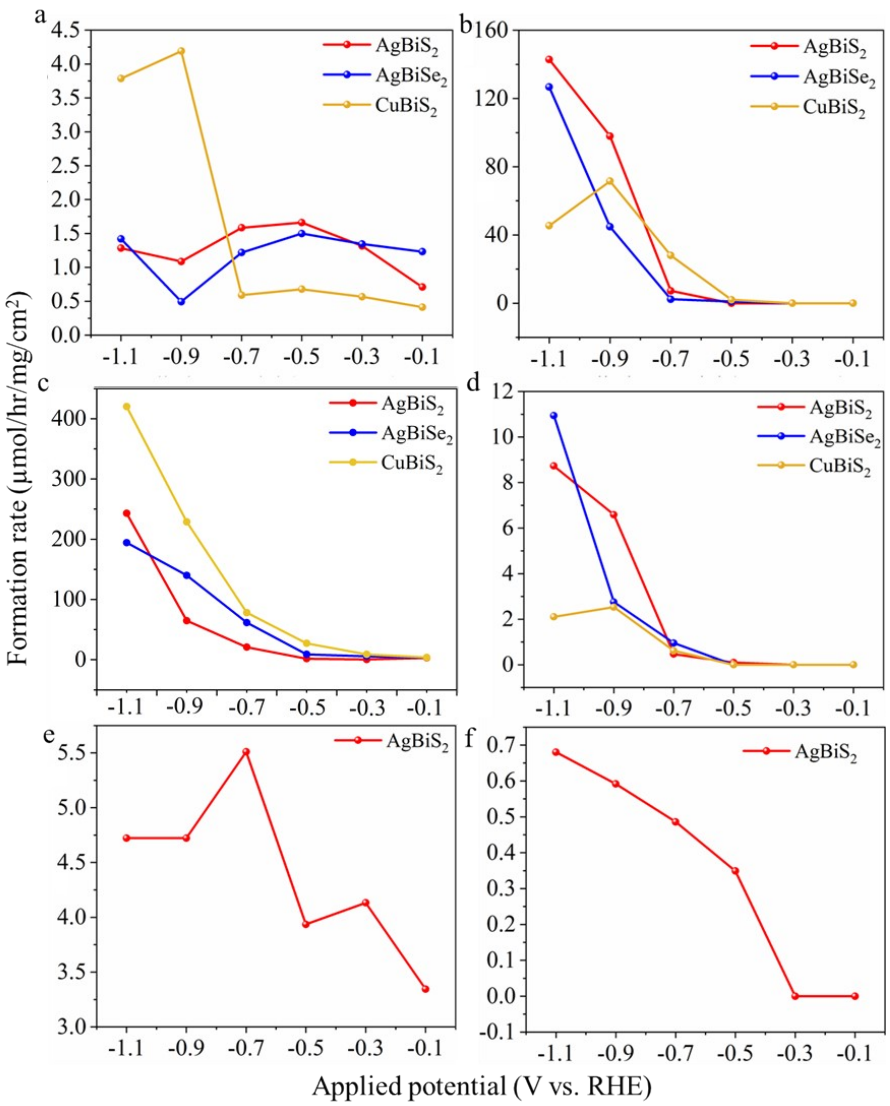

Figure S23. Formation rate of each CO_2 reduced products **(a)** acetic acid, **(b)** formic acid, **(c)** hydrogen, **(d)** carbon monoxide, **(e)** methanol and **(f)** methane as a function of potential during eCO_2RR on $AgBiS_2$, $AgBiSe_2$ and $CuBiS_2$ catalysts. Methanol and methane were selectively produced on $AgBiS_2$.

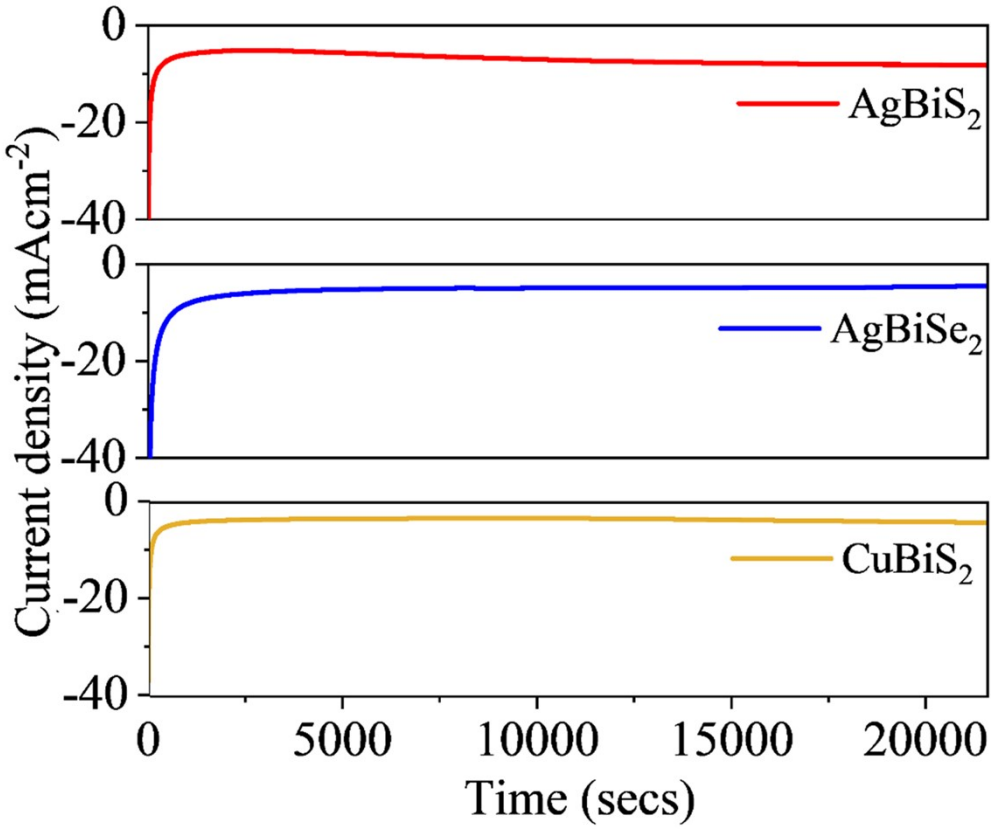

Figure S24. Chronoamperometry for $AgBiS_2$, $AgBiSe_2$ and $CuBiS_2$ at potential of -0.3 V vs. RHE in CO_2-saturated 0.5 M $KHCO_3$ in eCO_2RR for 6 h.

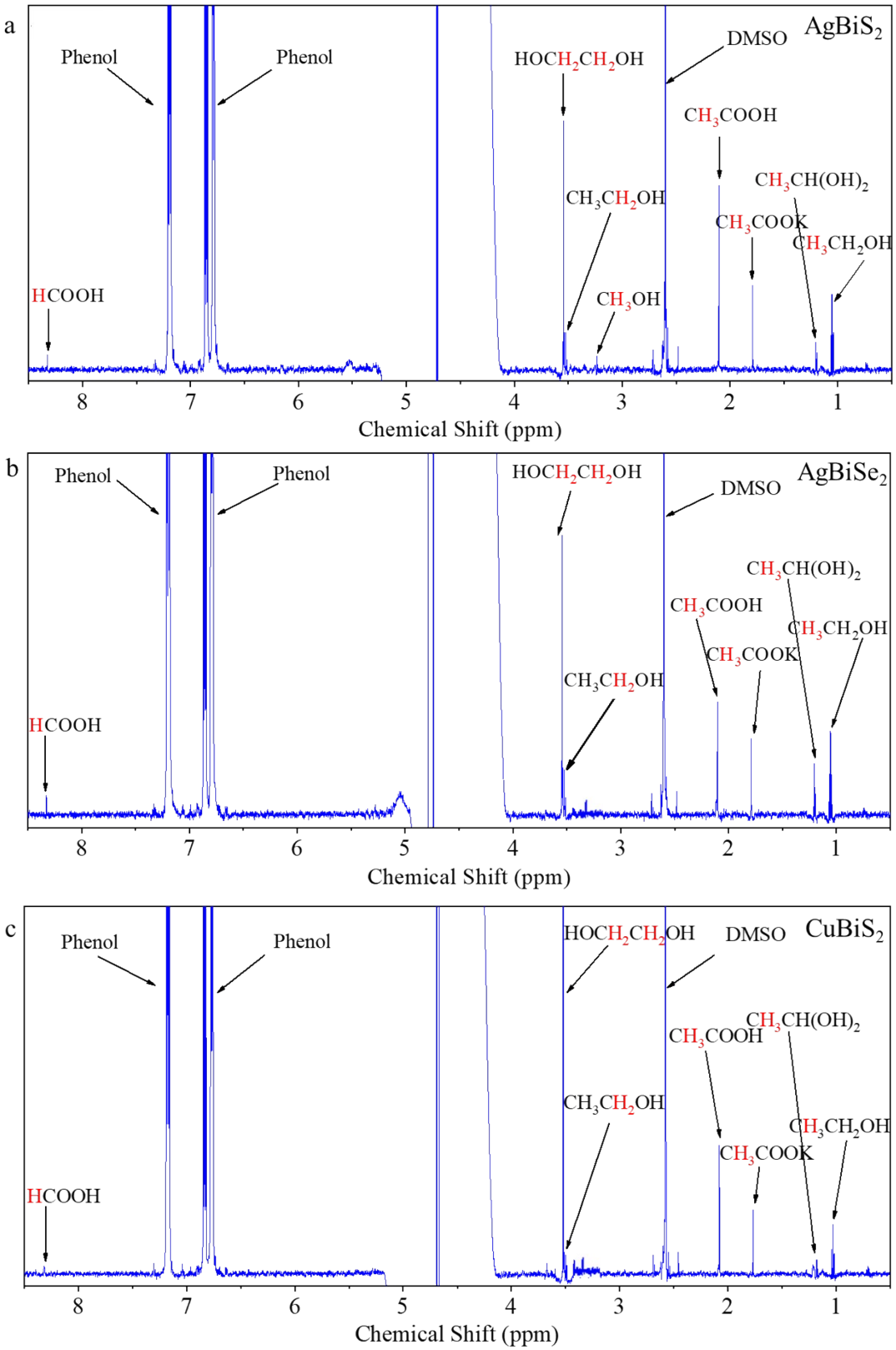

Figure S25. NMR spectra of the catholyte obtained from the CO_2 reduction at potential of -0.3 V vs. RHE for **(a)** $AgBiS_2$, **(b)** $AgBiSe_2$ and **(c)** $CuBiS_2$. Experimental conditions: $AgBiS_2$, $AgBiSe_2$ and $CuBiS_2$ as working electrode with 0.5 M $KHCO_3$ electrolyte at the end of six hours of CA measured at potential of -0.3 V vs. RHE.

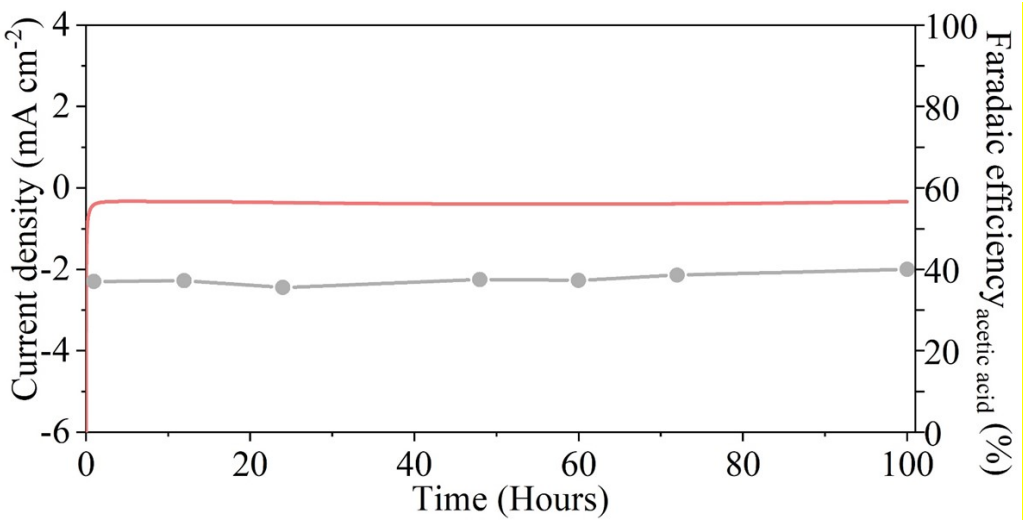

Figure S26. Chronoamperometry and Faradaic efficiency of acetic acid versus time for $AgBiSe_2$ catalyst at a potential of -0.3 V vs. RHE in CO_2-saturated 0.5 M $KHCO_3$ in eCO_2RR for 100 h.

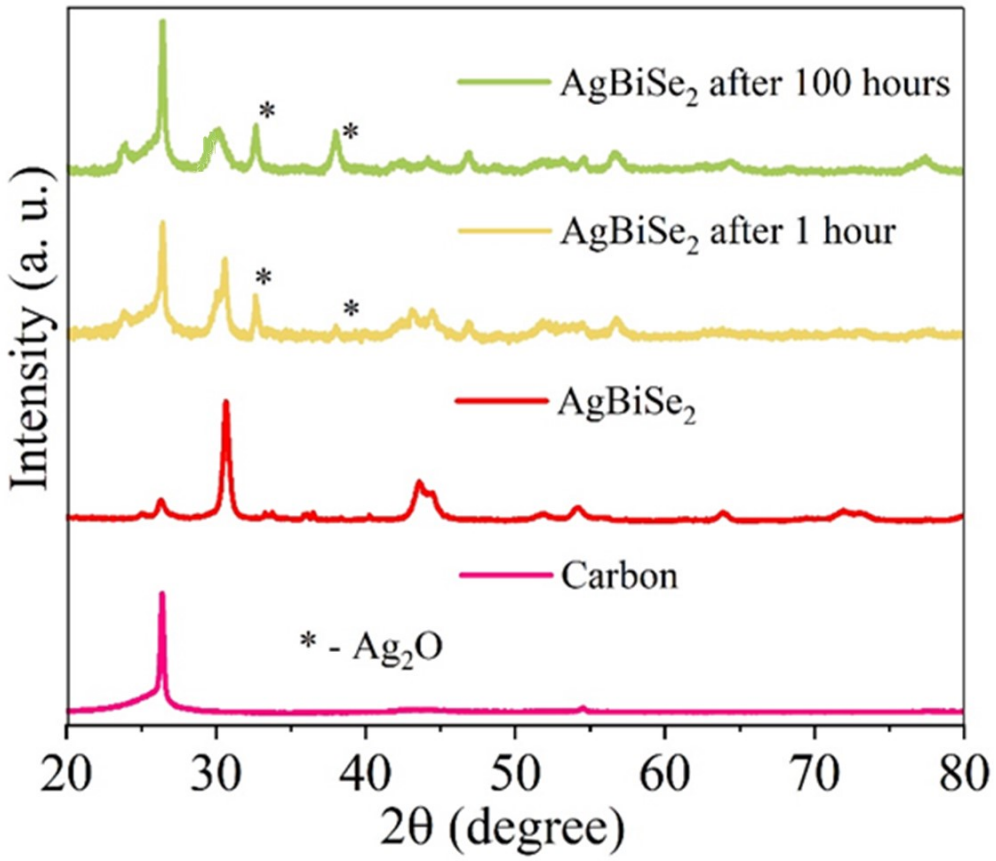

Figure S27. Post electrochemical XRD analysis of $AgBiSe_2$ recorded after prolonged electrolysis upto 100 hours at a potential of -0.3V vs. RHE.

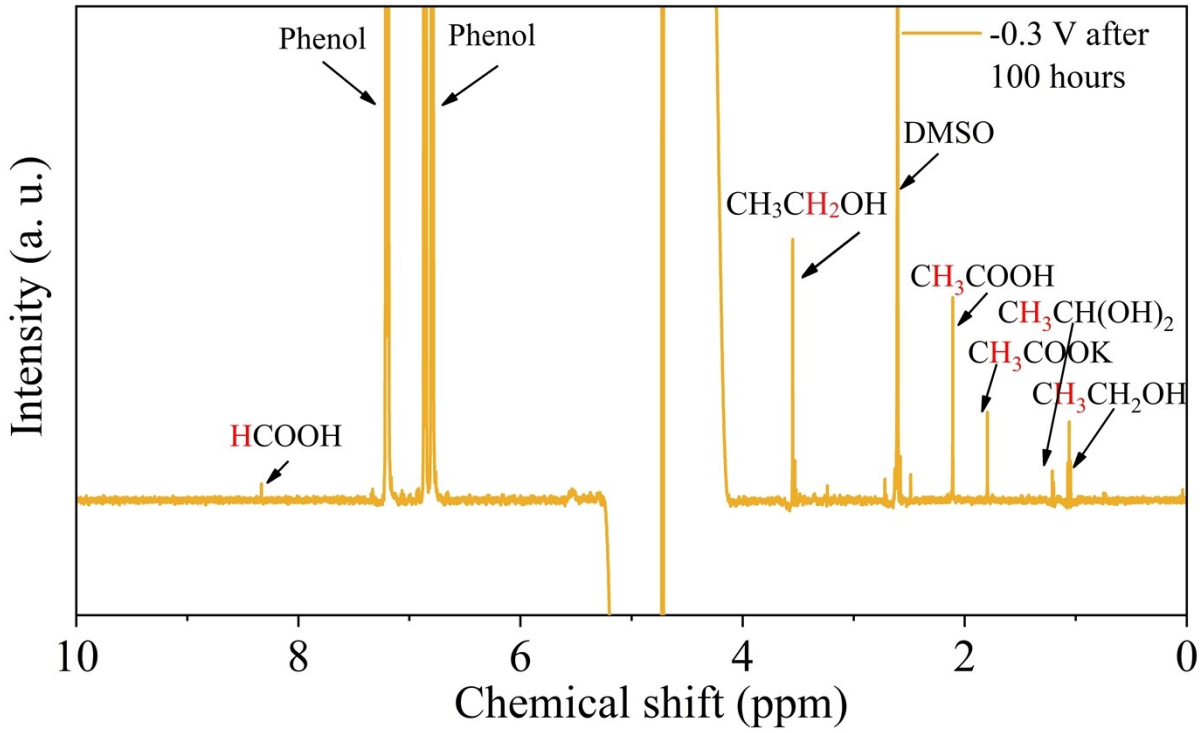

Figure S28. NMR spectra of the catholyte obtained from the CO_2 reduction at potential of -0.3 V vs. RHE for $AgBiSe_2$ at the end of 100 hours of electrolysis at a potential of -0.3V vs. RHE.

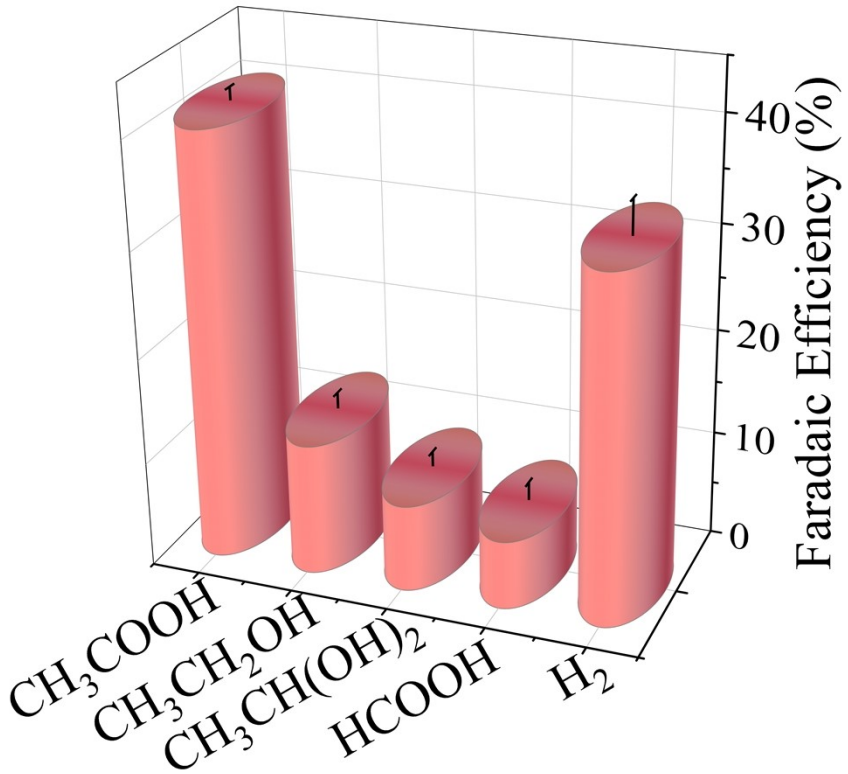

Figure S29. Faradaic efficiency for each CO_2 reduced major liquid and gaseous products on $AgBiSe_2$ at a potential of -0.3 V vs. RHE in CO_2-saturated 0.5 M $KHCO_3$ in eCO_2RR for 100 h.

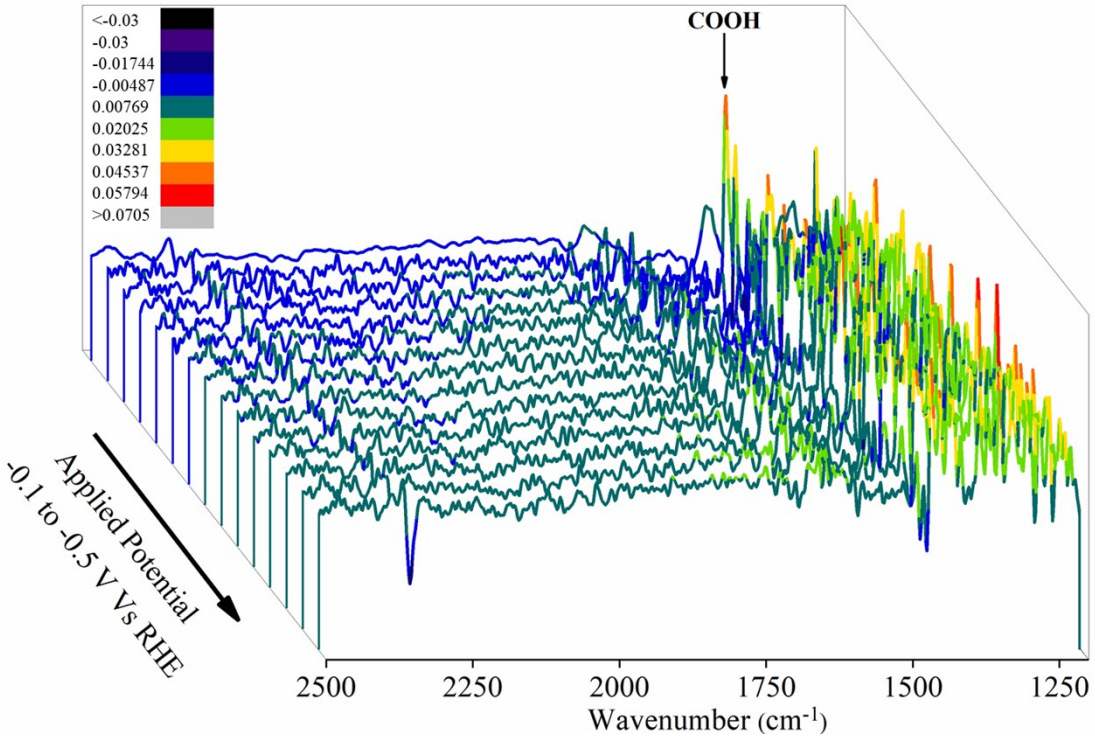

Figure S30. In situ ATR-IR spectra of CO_2 reduction on $AgBiS_2$ electrode at applied potentials ranging from -0.1 to -0.5 V Vs RHE.

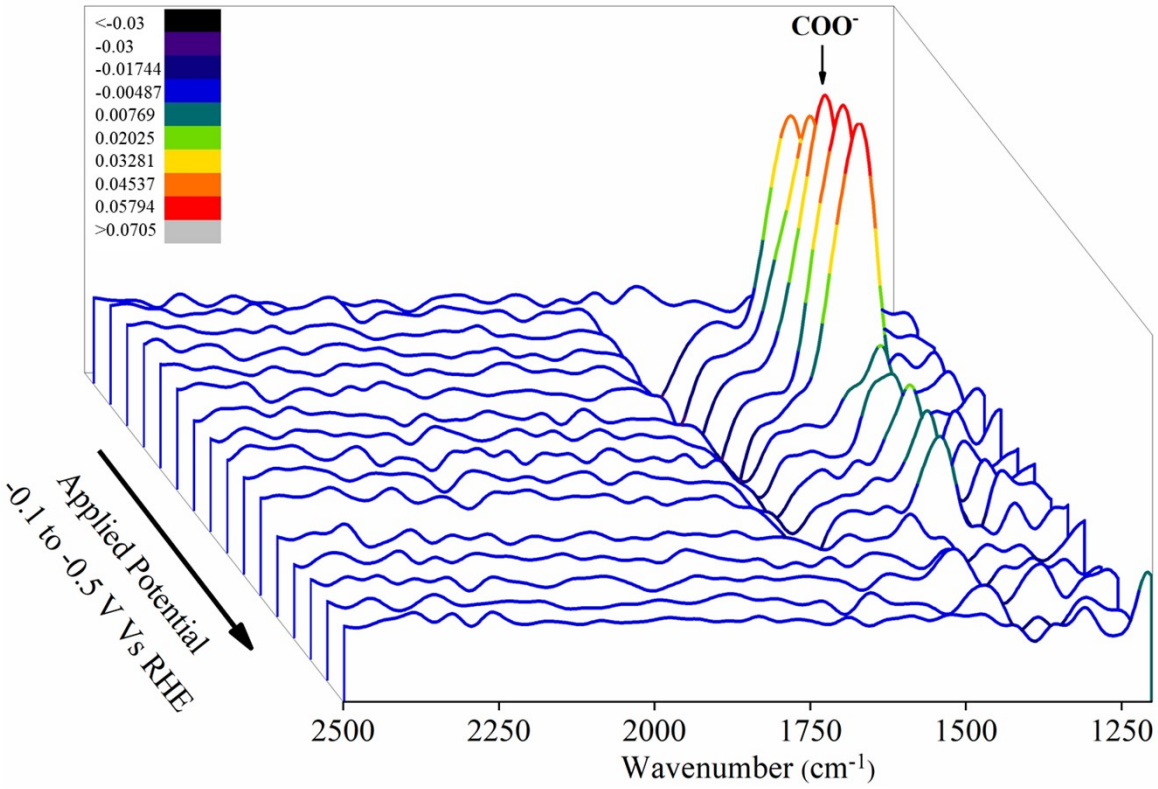

Figure S31. In situ ATR-IR spectra of CO_2 reduction on $AgBiSe_2$ electrode at applied potentials ranging from -0.1 to -0.5 V Vs RHE.

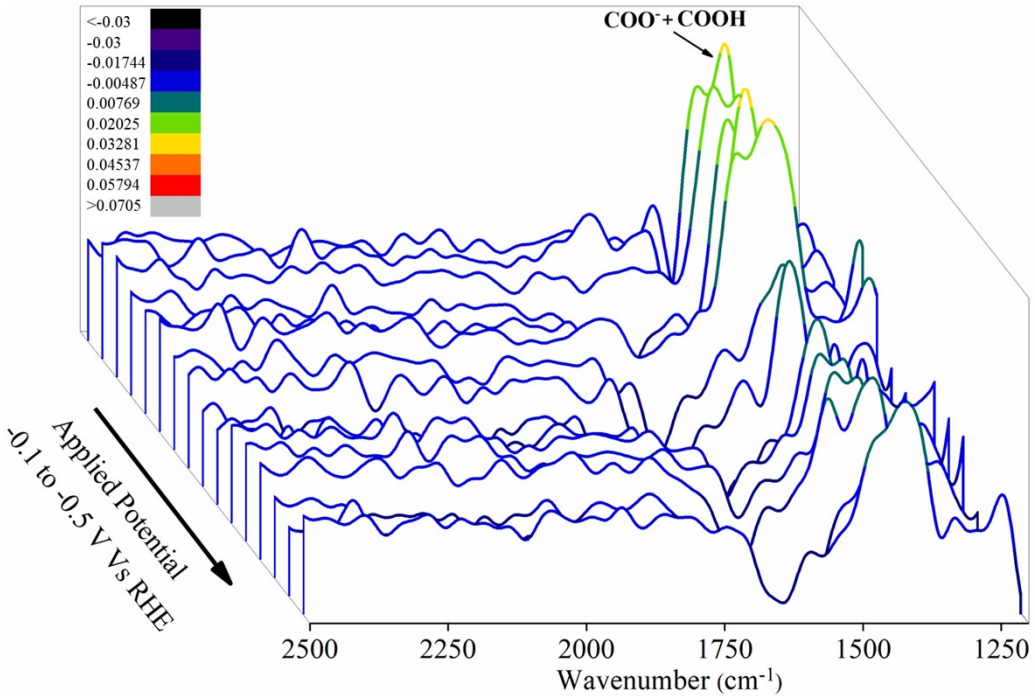

Figure S32. In situ ATR-IR spectra of CO_2 reduction on $CuBiS_2$ electrode at applied potentials ranging from -0.1 to -0.5 V Vs RHE.

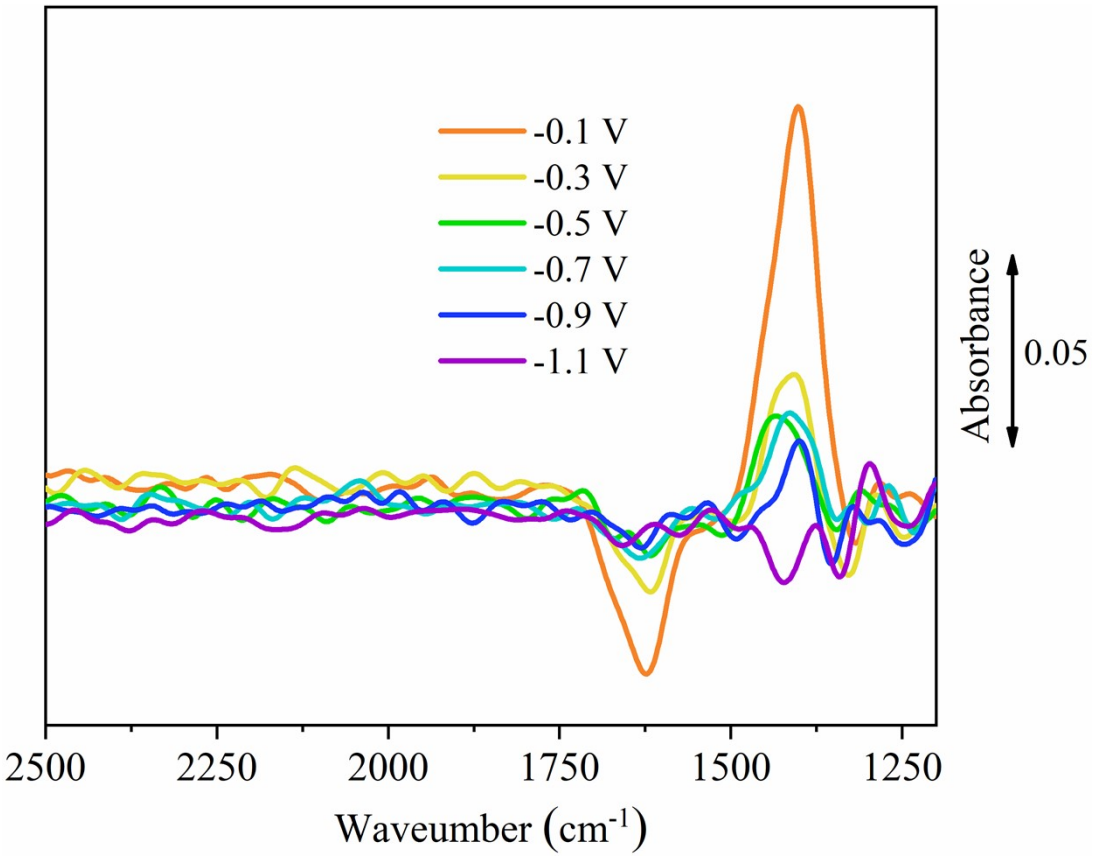

Figure S33. In situ ATR-IR spectra of CO_2 reduction on $AgBiSe_2$ electrode at applied potentials ranging from -0.1 to -1.1 V Vs RHE.

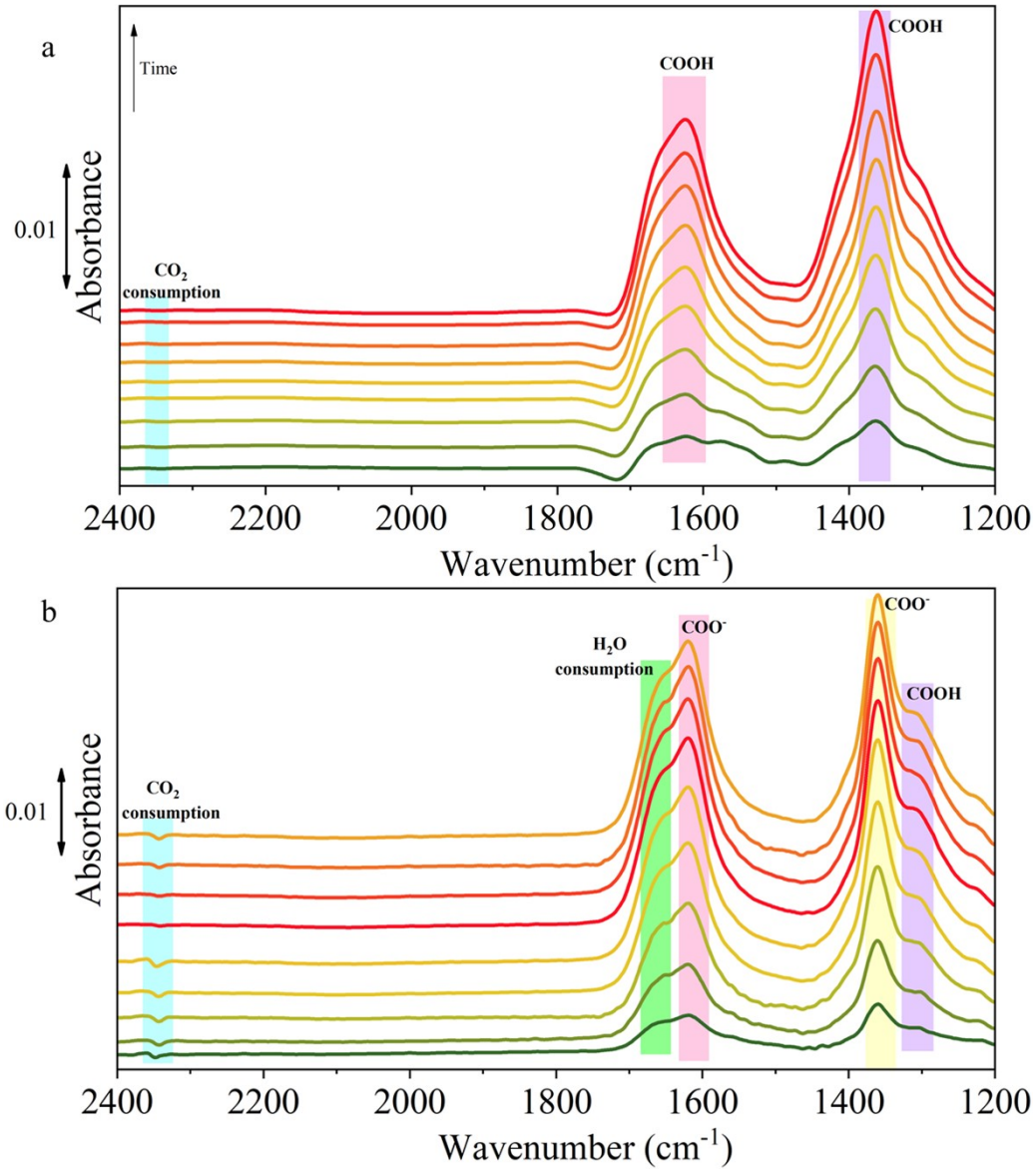

Figure S34. In situ ATR-IR spectra during electrochemical CO_2 reduction on (a) $AgBiS_2$ and (b) $AgBiSe_2$ electrodes respectively at potential of -0.1V vs. RHE in 0.1M KCl.

In case of $AgBiS_2$ (Figure S34a) the broad peak at 1362 cm^{-1} corresponds to the overlapped peaks due to carbon bound *COO^- intermediate and C-O stretch of COOH. At 1625 cm^{-1} the peak corresponding to C=O stretch of COOH intermediate appears.[1,2]

A strong band appears at 1395 cm^{-1} (Figure S34b) indicating the symmetric stretch mode of carbon bound *COO^- intermediate. The slight hump at 1306 cm^{-1} is assigned to the OH deformation of COOH. Water consumption associated with the HER is indicated by the H-O-H band at 1647 cm^{-1}. This peak may be overlapping with the C=O stretch of *COOH intermediate as seen from the slight hump at 1620 cm^{-1}.

In both the cases CO_2 consumption peaks appears around 2348 cm^{-1}.[1,2]

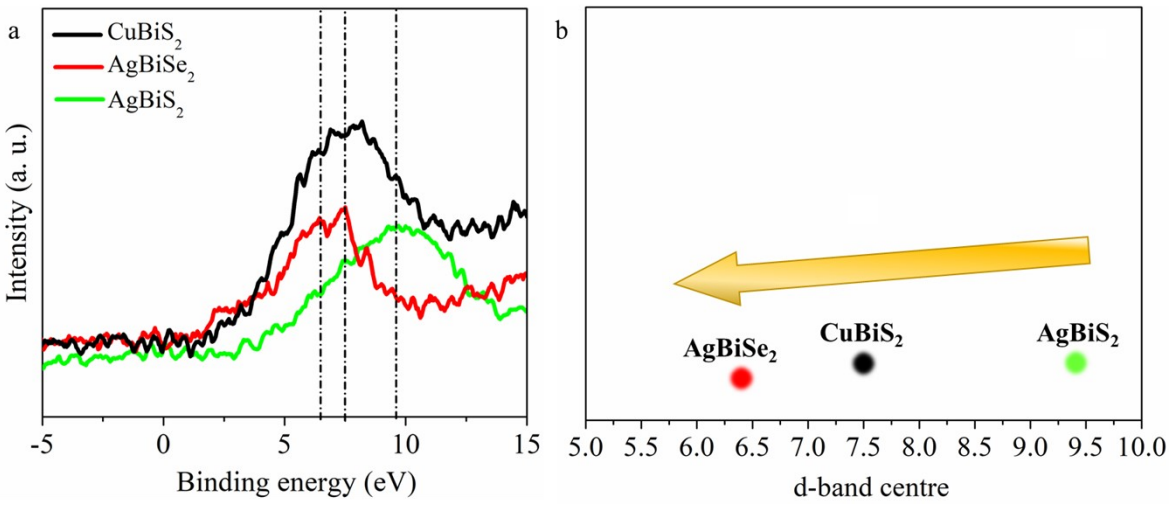

Figure S35. (a) XPS valence band spectra collected from $AgBiS_2$, $AgBiSe_2$ and $CuBiS_2$ nanoparticles and **(b)** change in d-band center as observed from XPS valence band spectra.

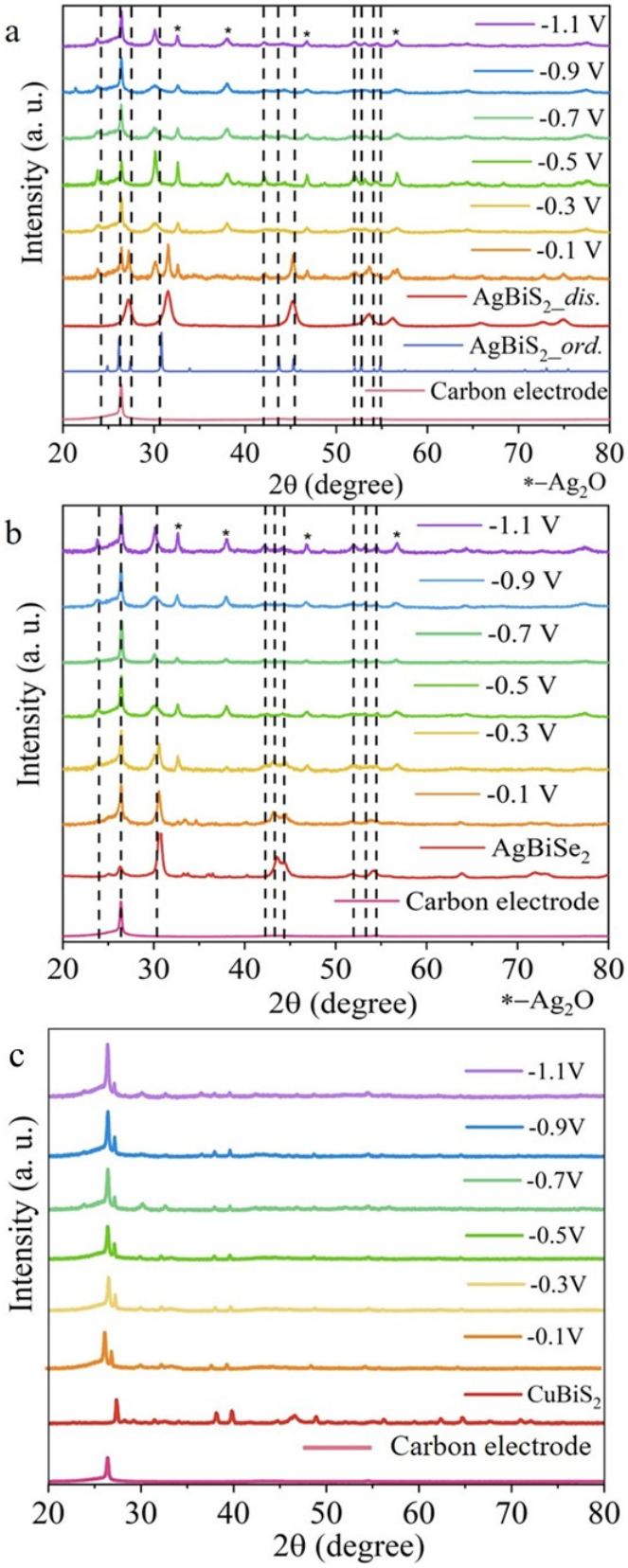

Figure S36. Post electrochemical XRD analysis of **(a)** $AgBiS_2$, **(b)** $AgBiSe_2$ and **(c)** $CuBiS_2$ recorded after eCO_2RR at each potential.

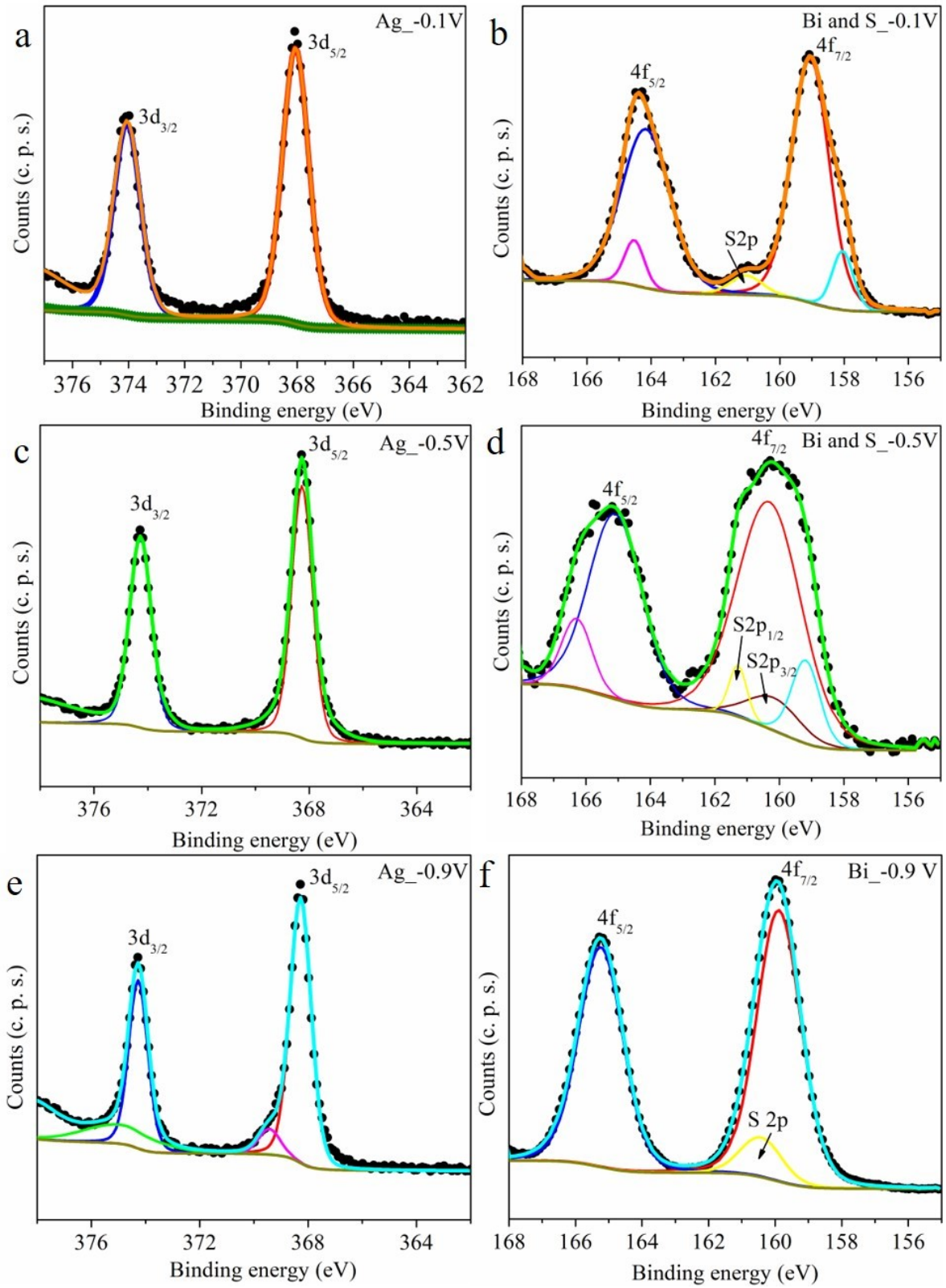

Figure S37. Post electrochemical XPS analysis of $AgBiS_2$ recorder after eCO_2RR at each potential.

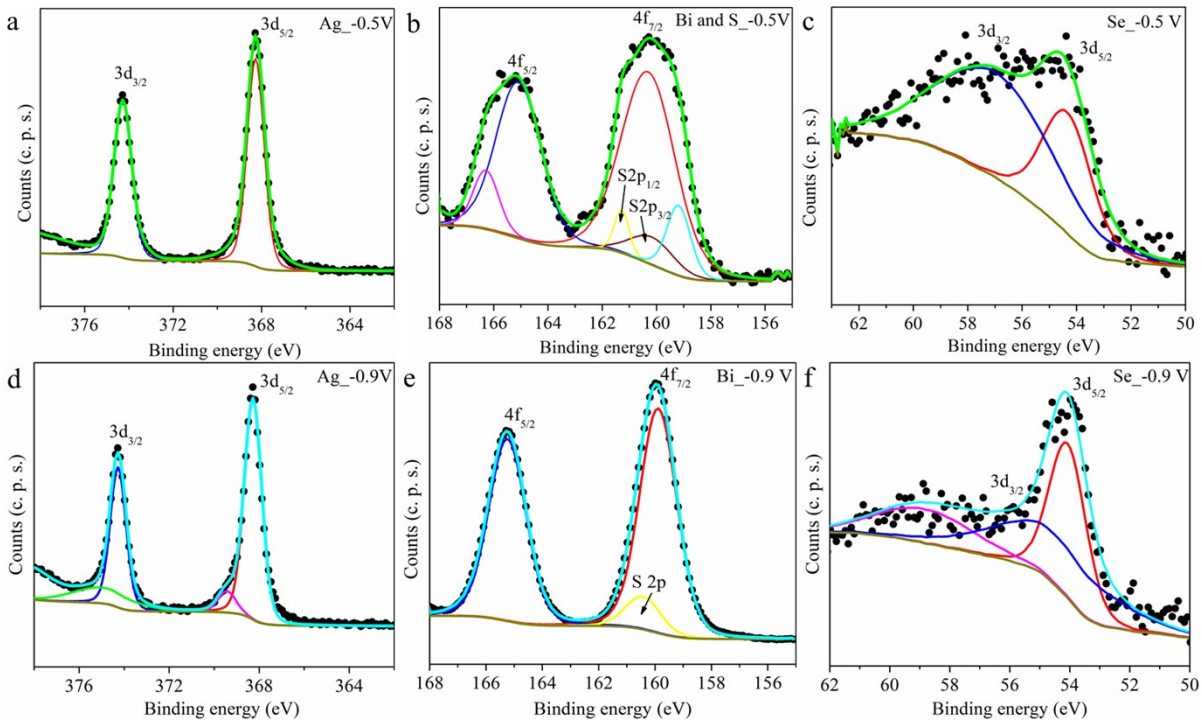

Figure S38. Post electrochemical XPS analysis of $AgBiSe_2$ recorder after electrolysis at each potential.

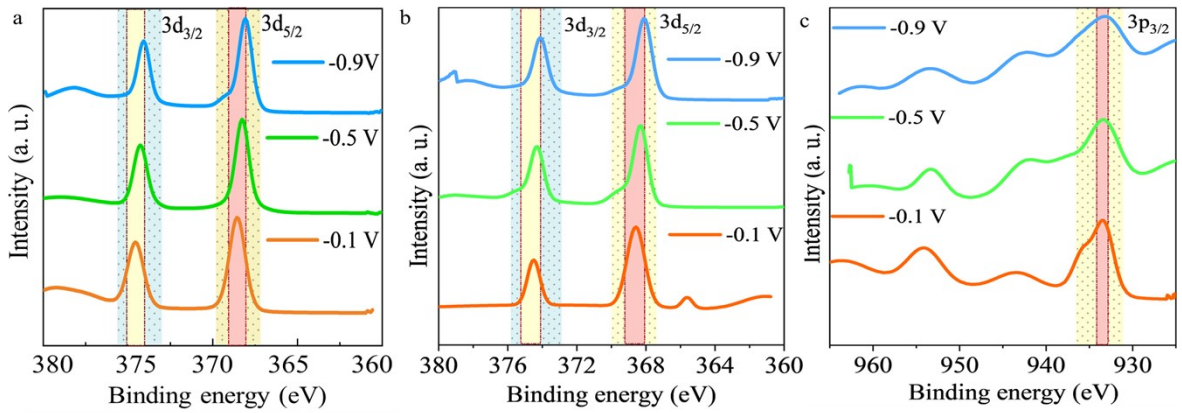

Figure S39. Post electrochemical CO_2RR XPS spectra at varying potentials for **(a)** $AgBiS_2$: Ag edge, **(b)** $AgBiSe_2$: Ag edge and **(c)** $CuBiS_2$: Cu edge.

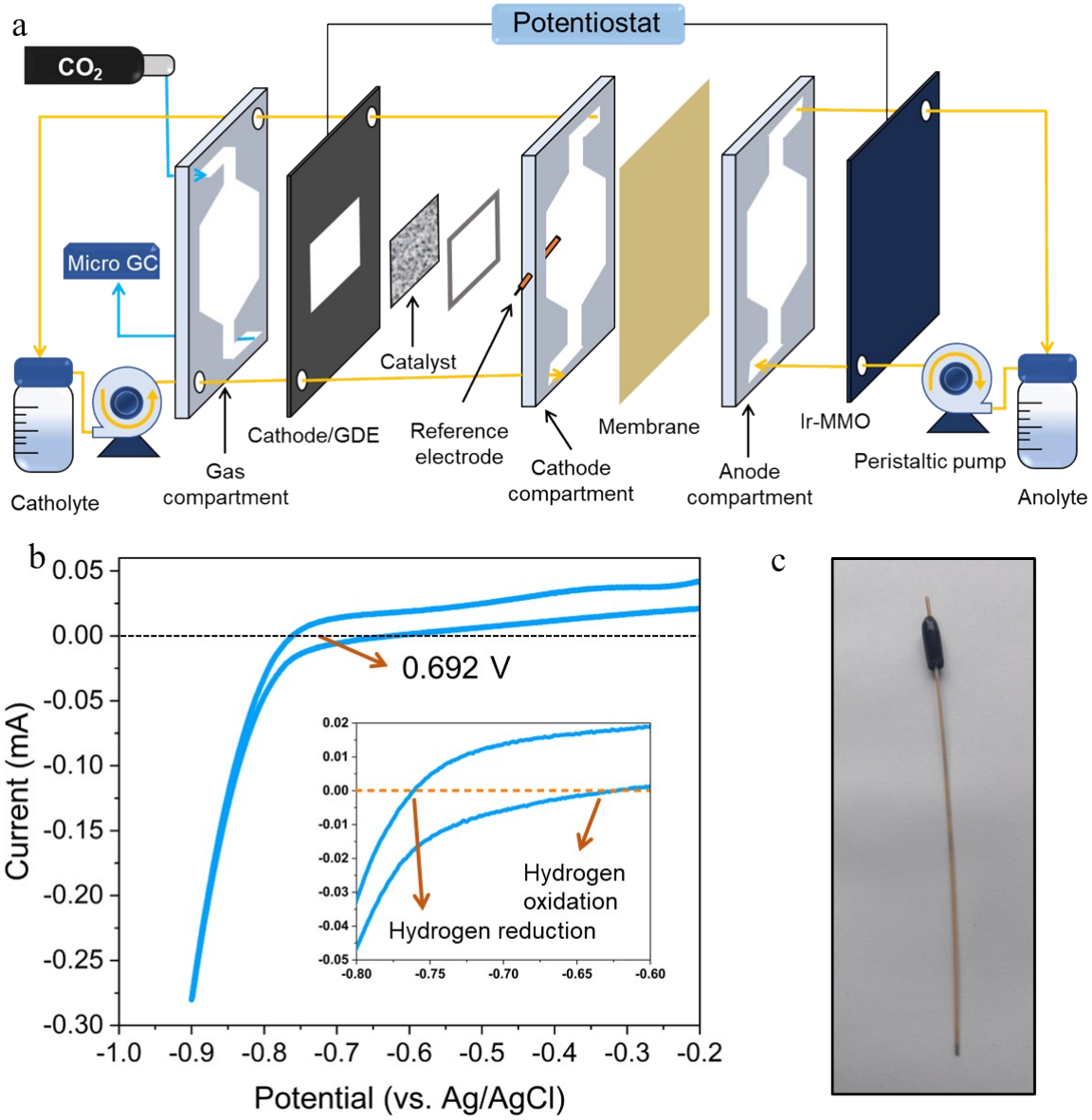

Figure S40. (a) Schematic illustration of Flow-cell used in the electrochemical CO_2 reduction. (b) RHE calibration of Ag/AgCl electrode under hydrogen saturated 0.5M $KHCO_3$. (c) Photograph of the Ag/AgCl electrode (reference) used in flow cell configuration.

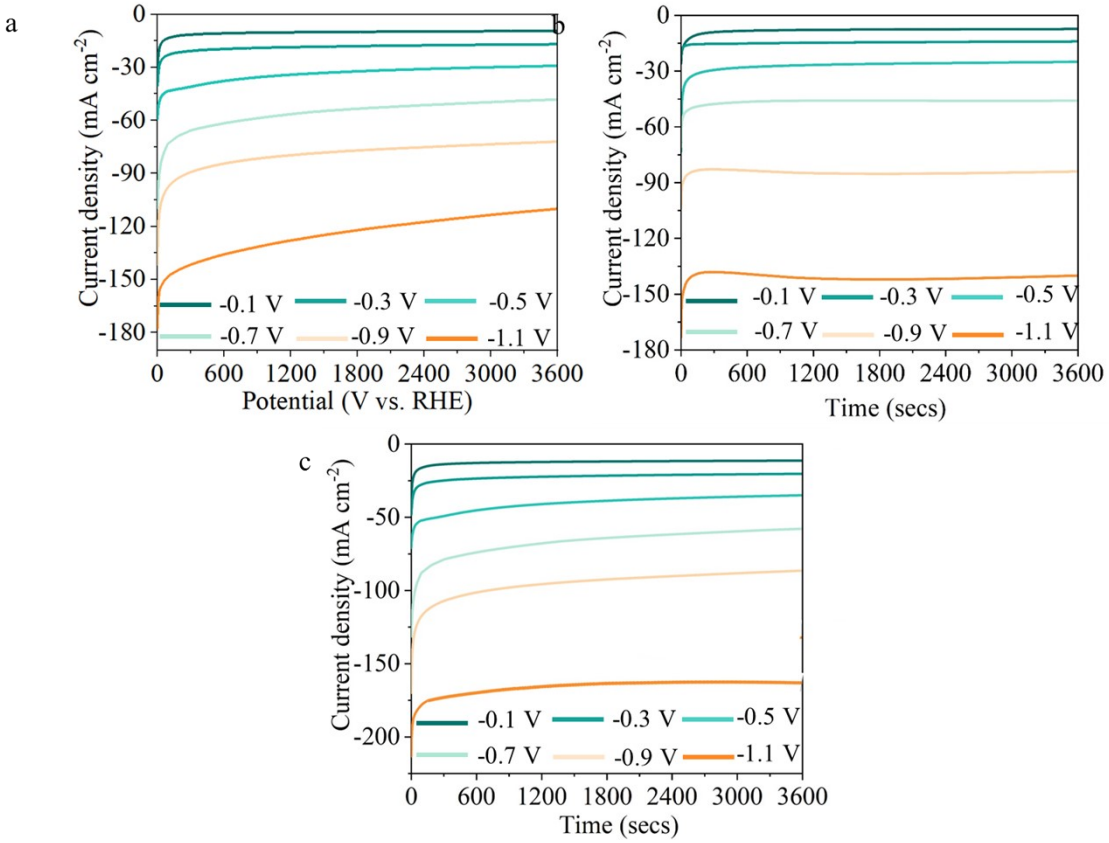

Figure S41. Chronoamperometric study on (a) $AgBiS_2$ and (b) $AgBiSe_2$ and (c) $CuBiS_2$ catalysts during electrochemical CO_2RR using flow cell in 0.5M $KHCO_3$.

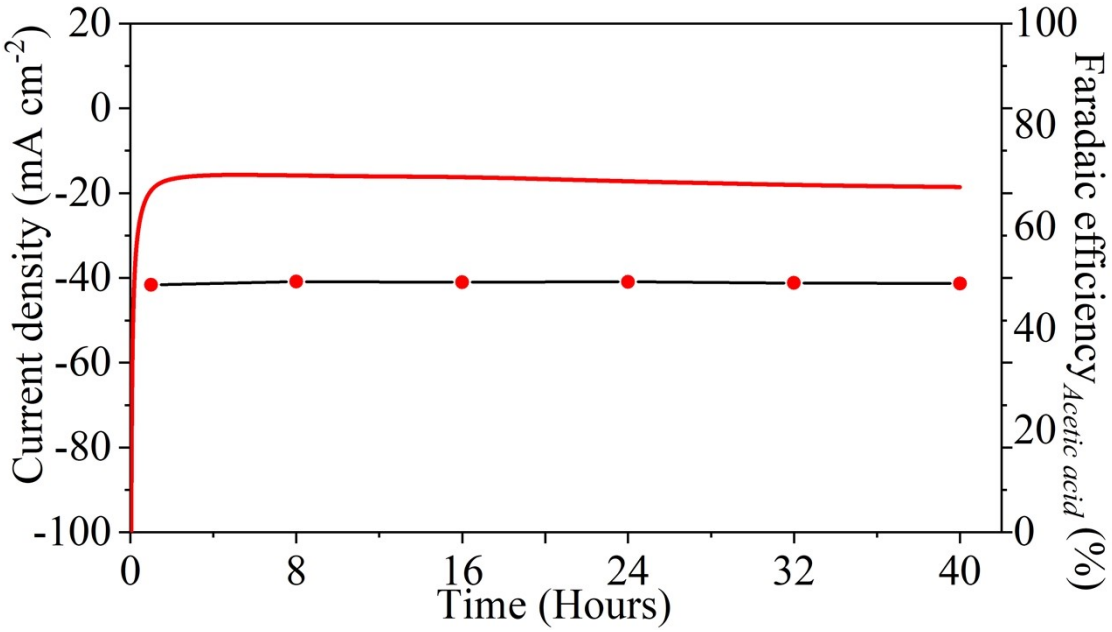

Figure S42. Chronoamperometric stability study on $AgBiSe_2$ at -0.3 V (vs. RHE) and FE of acetic acid in flow cell configuration in CO_2RR condition.

Notes

Notes S1: Figure S7 shows the XPS spectra of $AgBiS_2$ and $CuBiS_2$ respectively. Binding energy values of 368 eV and 375 eV in Figure S7a arises due to $3d_{5/2}$ and $3d_{3/2}$ spin-orbit coupling states of Ag in $AgBiS_2$ whereas Bi $4f_{7/2}$ and $4f_{5/2}$ spin states (**Figure S7b**) are demonstrated by binding energies corresponding to 157.5 eV and 162.5 eV respectively. In $CuBiS_2$ (**Figure S7c** and **S7d**) binding energy values of 933 eV and 953 eV correspond to $2p_{3/2}$ and $2p_{1/2}$ spin-orbit coupling states of Cu and also show the presence of copper oxide satellite peaks at 960 eV and 980 eV, respectively. However, Bi $4f_{7/2}$ and $4f_{5/2}$ spin states appear at slightly higher binding energy of 158 eV and 163 eV, respectively.

XPS spectra of $AgBiSe_2$ have been shown in **Figure S8**. Ag $3d_{5/2}$ and $3d_{3/2}$ spin-orbit states correspond to binding energies of 367.5 eV and 374.6 eV respectively (**Figure S8a**). F**igure S8b** shows the presence of Bi $4f_{7/2}$ and $4f_{5/2}$ spin states whereas binding energies of 55.4 eV and 56 eV in **Figure S8c** correspond to Se 3d spin-orbital coupling. The presence of slight amount of SeO_2 was also detected due to slight surface oxidation.

Comparison of Ag 3d XPS spectra of $AgBiS_2$ and $AgBiSe_2$ shows an upward shift in binding energy of Ag in $AgBiS_2$ attributed to the lower electronegativity of Se in comparison to that of S (**Figure S9a**). Hence, changing the chalcogenide anion from S to Se results in wider charge separation in $AgBiS_2$. Additionally, comparison of Bi 4f XPS spectra (**Figure S9b**) also demonstrates a shift towards higher binding energy in case of $AgBiS_2$. However, Bi 4f XPS spectra of $CuBiS_2$ exhibit a positive shift in binding energy with respect to both $AgBiS_2$ and $AgBiSe_2$. The higher electronegativity of Ag in comparison to that of Cu rationalizes this observation. Hence, it can be concluded that changing the cationic and anionic counterparts causes significant changes in the localized electron distribution.

Notes S2. Ag *K*-edge XANES spectra show an increase in absorption edge and white-line intensity for $AgBiS_2$ in comparison to that of $AgBiSe_2$ (**Figure S10a**). Increase in white line

intensity and absorption edge is indicative of increase in the unoccupied d-orbital states of adjacent metal centers and this induces positive charge at the metal centre. Comparison of Bi-L_{III} edge XANES spectra for all the three catalysts showed that $CuBiS_2$ exhibited the highest white line intensity (**Figure S10b**). Concisely we can predict that replacing Ag and S in $AgBiS_2$ with Cu and Se respectively resulted in variation of lattice charge due to lower electronegativity of Se in comparison to that of S and higher electronegativity of Ag as compared to that of Cu.

Notes S3. At the end of each CA, catholyte has been taken out and analyzed by 1H NMR. In case of $AgBiS_2$, the liquid products consist of formic acid (δ = 8.295, s, 1H), methanol (δ = 3.189, s, 3H) and acetic acid (δ = 2.05, s, 3H) (**Figure S18)**. DMSO and phenol has been added into the catholyte as the internal standards and appeared at δ = 2.56 ppm and δ = 6.74-7.15 ppm respectively. The NMR spectra of liquid product of $AgBiSe_2$ (**Figure S19**) show formic acid (δ = 8.295, s, 1H), in the higher potential (−0.7 V to −1.1 V) and acetic acid (δ = 2.05, s, 3H) in predominantly in the lower applied potential. FE for respective products as a function of potential have been derived from the peak area obtained in the NMR spectra. The NMR spectra of liquid product of $CuBiS_2$ (**Figure S20**) show formic acid (δ = 8.295, s, 1H), in the higher potential (−0.7 V to −1.1 V) and acetic acid (δ = 2.05, s, 3H) in almost every potential. FE for HCOOH and CH_3COOH were found to be less in case of $CuBiS_2$ is evident from the peak area obtained in the NMR spectra.

References

[1] Zhu, S.; Li, T.; Cai, W.-B.; Shao, M. *ACS Energy Lett.* **2019**, *4*, 682-689.
[2] Firet, N. J.; Smith, W. A. *ACS Catal.* **2017**, *7*, 606-612.
[3] R. De, S. Gonglach, S. Paul, M. Haas, S. S. Sreejith, P. Gerschel, U.-P. Apfel, T. H. Vuong, J. Rabeah, S. Roy and W. Schöfberger, *Angew. Chem*. **2020**, *59*, 10527-10534.
[4] Y. Liu, S. Chen, X. Quan and H. Yu, *J. Am. Chem. Soc*., **2015**, *137*, 11631-11636.
[5] B. Zha, C. Li and J. Li, *J. Catal*., **2020**, *382*, 69-76.
[6] X. Sun, Q. Zhu, X. Kang, H. Liu, Q. Qian, J. Ma, Z. Zhang, G. Yang and B. Han, *Green Chem*., **2017**, *19*, 2086-2091